# Characterization of inclusions and their distribution in natural and artificial ice samples by synchrotron cryo-micro-tomography (SCXRT)

Dissertation
zur Erlangung des Grades
„Doktor der Naturwissenschaften“

am Fachbereich für Chemie, Pharamazie und Geowissenschaften
der Johannes Gutenberg Universität

Markus Maria Miedaner
geb.: 11.09.1978 in Ingolstadt

Mainz, 2007.

Dekan: XXX

1. Berichterstatter: XXX
2. Berichterstatter: XXX

Tag der mündlichen Prüfung: 15.05.2007

zieh deinen weg - folg deinen eigenen regeln
zieh deinen weg - keine angst vor richtig und falsch
wer die wahrheit kennt - ist niemals überlegen
vertritt deinen punkt - aber zeug immer von respekt
verrat dich nicht - beharrlichkeit ist eine tugend
verstell dich nicht - verfolge still dein ziel
spiegel dich - deinen vorteil, deine jugend
schärf deinen blick - vergib vertrauen immer zuletzt
sei aus unsicherheit nicht arrogant - hab immer mitgefühl als unterpfand
stell dich jedem konflikt mit leichter distanz - sei bereit zum kompromiss
führe, wo es zu kämpfen gilt - niemals verschlagenheit im schild
tu nicht ungefragt, was alle tun - alle hat kein gesicht
zieh deinen weg - als freier radikaler
zieh deinen weg - sei unvorsichtig, verrückt
zier dich nicht - irrtum ist keine falle
verschenk dein herz - und nimm es auch wieder zurück
lass dir niemals dein lachen stehln - auch wenn dir manchmal die gründe fehln
hab keine angst vorm lächerlich sein - schüchtern ist das neue forsch
...

*zieh deinen weg* aus "12" - Herbert Grönemeyer - 2007

# Contents

# List of Tables

# List of Figures

# Zusammenfassung

Zur geometrischen Vermessung und Beschreibung von Einschlüssen in natürlichen sowie im Labor geschaffenen Eispartikeln wurde ein neuartiger Versuchaufbau an der Tomographie-Endstation der Material Science Beam Line an der Swiss Light Source (SLS, Paul Scherrer Institut, Villigen, Schweiz) entwickelt. Dieser besteht aus einer Plexiglas-Tasse und einem doppelwandigen Kaptonfolien-Käfig, der wiederum auf die Düse eines CryojetXL (Oxford Instruments) montiert wurde. Abgesehen von dem hohen Maß an Flexibilität bezüglich der Installation erlaubt es dieser Aufbau, die Temperatur des Experiments mit einer Genauigkeit von ± 1 K über einen Bereich von 271 K bis 220 K zu regeln. In den hier beschriebenen Experimenten wurde eine räumliche Auflösung von 1.4 $\mu$m erzielt.

In natürlichen Proben, die an verschiedenen Orten gesammelt wurden, konnten nur Luftblasen gefunden werden. Weitere Verunreinigungen, wie z.B. Säuren oder Mineralstaub, waren entweder in zu geringer Konzentration vorhanden und erzielten so keinen ausreichenden Adsorptionskontrast, oder waren deutlich kleiner als die räumliche Auflösung der Messaparatur. Ein Teil der natürlichen Proben wurde zur Metamorphose bei höheren Temperaturen gezwungen. Damit konnten bisherige Studien über die isotherme und gradienten getriebene Eis-Metamorphose um die Veränderung der inneren Oberfläche erweitert werden. Ein vergleichbares Experiment wurde mit einer verdünnten Salzlösung durchgeführt um den Transport der Verureinigungen entlang der Eiskorngrenzen zu charakterisieren.

In einem zweiten Experiment wurden Tropfen einer verdünnten NaBr-Lösung unter nahezu atmospherischen Bedingungen bei verschiedenen Temperaturen (271 - 203 K) ausgefroren, um die Änderung des Einschlussvolumens und seiner Morphologie in Abhänigkeit von der Temperatur zu untersuchen. Die größten Strukturen wurden bei 271 K und bei 203 K gefun-

den. Mit Hilfe eines statistischen Ansatzes, der *Crystal Size Distribution - CSD*, wurden die Nukleations- und Wachstumsraten der verschiedenen Einschlusstypen aus den tomographischen Daten extrahiert. Die höchste Keimbildungs- und Wachstumsrate wurde für Gefrierprozesse bei 240 K gefunden.

Die Interaktion verschiedener Aerosol-Proxy-Substanzen miteinander während des Gefrierens sind im letzten Experiment untersucht worden. Dafür wurden Octanol, NaBr-Lösung, Mineralstaub und MilliQ-Wasser in bestimmten Verhältnissen mit einander gemischt. Besonders die Kombination von Octanol mit einer schwach salzhaltigen Lösung zeigte die Ausbildung eines sich über die ganze Probe erstreckenden Netzwerkes des NaBr-Octanol-Gemisches. Ähnliches ergab auch die Beimischung von Bentonit zu einer schwach salzhaltigen Lösung. Solche Netzwerke verändern deutlich die Reaktivität des Eispartikels in Hinblick auf die ihn umgebende Gasphase und können vor allem in Seeeis oder in Gletschern für einen ungehinderten Transport von Stoffen sorgen.

Zusammenfassend lässt sich festhalten, dass sich mit dem neu entwickelten Versuchsaufbau verschiedenste Proben bei Temperaturen von 271 K bis 220 K bei einer räumlichen Auflösung von 1.4 $\mu$m in circa 90 Minuten untersuchen lassen. In den Metamorphoseexperimenten wurde zudem bereits der erste Ausblick auf die zukünftige, zeitaufgelöste Tomographie (4D-Tomographie) gegeben.

## Abstract

To characterize trapped inclusions in natural as well as artificial ice particles a new setup has been developed at the tomography end-station of the material science beam line at the Swiss Light Source (Paul Scherrer Institut, Villigen, Switzerland). It mainly consists of a custom-made polyamide cup and a double-walled Kapton-foil cage mounted onto the nozzle of a CryojetXL (Oxford Instruments). Besides its high degree of portability, this setup also allows controlling the experimental temperature with an accuracy of $\pm$ 1 K in a range from 271 K to 220 K. A spatial resolution of 1.4 $\mu$m was obtained in the presented experiments.

In natural samples (hail stones from different locations) only air-filled voids could be seen, because other impurities like acids or mineral dust were at such low concentrations that they did not yield any detectable adsorption contrast, or these inclusions were of a size well below the spatial resolution. Given the good thermal precision and the flexibility of the setup a natural sample as well as a specimen frozen from a diluted NaBr solution were forced to metamorphose by heating them. Due to heating a significant transport of impurities along the grain boundaries between ice crystals was found. The occurring changes in the internal surface area agree well with studies on the metamorphism of the outer surface of snow. So previous studies could be extended to the inside of atmospheric ice particles. Furthermore, this experiment represents the first step towards time-resolved tomography, which had not been possible with the experimental setups described in the literature so far.

In a second experiment droplets of a diluted NaBr solution were frozen at different exposure temperatures ranging from 270 K to 203 K under conditions mimicking atmospheric ones. The changes in morphology and size of the trapped inclusions and phases in the resulting polycrystalline ice sphere were investigated. The largest inclusions were found at the highest

(271 K) as well as at the lowest (203 K) exposure temperature. Using a statistical approach, *Crystal Size Distribution - CSD*, the nucleation and growth rates for the air- as well as for the salt-filled voids could be deduced from the experimental data. The nucleation and growth rates reached their maximum at an exposure temperature of 240 K.

In the last experiment the interaction of various aerosol proxies with each other during freezing was investigated. For this purpose octanol, a diluted NaBr solution, mineral dust, and MilliQ-water were mixed in certain ratios prior to freezing. Especially in the case of the Octanol-NaBr-formulation a well-connected network of inclusions developed throughout the sample. Similar structures were found by suspending Bentonite in a diluted NaBr solution. Such well-connected systems clearly influence the chemical and physical properties of an ice particle with respect to its surroundings, e.g. the uptake of gaseous substances. In sea ice as well as in glaciers connected voids not only host chemical reactions, but also allow the transport of impurities.

In conclusion, a new setup was developed to characterize the internal structure of various ice samples at well defined conditions (270 K - 220 K $\pm$ 1 K) within 90 minutes and a spatial resolution of 1.4 $\mu$m. The metamorphism experiments also gave the first glance at future time-resolved tomography experiments (4D-tomography).

# 1 Introduction

Natural ice forms as multiphase systems under various conditions. For example, in tropospheric clouds droplets of solutions of inorganic salts (e.g. sulfur dioxide, ammonium sulfate - typically at a $10^{-4}$ M concentration) and inorganic acids of several weight percent exist (1; 2; 3). Also organic acids have been found (4; 5; 6). Additionally, ice forms in brines of high concentration, such as sea water (3.5 wt.% NaCl) (7; 8). When it grows in those environments, most impurities are expelled from the crystalline matrix (9; 10). Hence, multi-phase systems are created, which consist of ice, solid salts, gaseous inclusions like air bubbles, highly concentrated inorganic as well as organic solutions and solid particles like mineral dust. Such systems are not only involved in the stratospheric and marine ozone chemistry (1; 2; 3; 7; 11) but also in cloud electricity, which may be enhanced by ionic impurities on the surface of atmospheric ice particles (12). Ice also occurs on the earth's surface. Here, polar and alpine ice act as important sinks for both volatile trace compounds and salt-containing aerosols from the ocean. Consequently, these reservoirs can be used to reconstruct paleoclimate (13; 14; 15). Such micro-phases may manifest in three dimensional networks within such ice accumulations. It has theoretically been predicted that significant amounts of impurities can be transported within those networks, even in very clean systems, such as ice cores (16).

Various chemical reactions take place on the interfaces between the trapped inclusions (4; 17; 18), inclusions and ice (19; 20; 21) as well as on the surface of ice particles. These not only alter the physico-chemical properties of the particles, but also involve the chemistry and physics of their surroundings. The chemical composition of trapped impurities controls the melting and solidification behavior of the sample as was investigated in great detail

by the research groups of Brimblecombe and Marion (7; 22; 23; 24; 25; 26; 27). The adsorption potential of gases onto the particle and their transport within the sample depend on the chemistry of the impurities, as a consequence of these phase changes. So far, the interaction between the gases and ice particles has been analyzed by weight-loss methods but rarely microscopically (28, and references therein).

Inclusions in atmospheric ice particles control how these particles scatter sunlight. For example, zones of high inclusion density cause a diffuse scattering. In mixed phase clouds as well as cirrus clouds these effects cause strong interactions with the climate. A detailed knowledge of the size- and spatial distribution of air bubbles in atmospheric ice particles would improve the current radiation models (29; 30; 31).

Like several semi-conductors, ice belongs to the group of surface-melting materials (32; 33). Such crystalline substances melt from the outside inwards. In the case of ice this is also causing the formation of a thin liquid film on its surface, the so called Quasi Liquid Layer (QLL) (34), at temperatures below its real melting point. The thickness of the quasi liquid layer in contact with the trapped impurity depends on the roughness of the interface and its chemistry (35; 36; 37). The environmental importance of this film has been highlighted by Voss et al. (38). Knowing the exact size and spatial distribution allows to venture first estimates about the thickness of the quasi liquid layer which determines further transport processes and interactions between different impurities.

In the cases of sea ice (8; 7) or permafrost soils (39; 40) freeze-thaw processes and the subsequent redistribution of the trapped inclusions are of key importance (41; 42). They not only determine which bacteria, insects etc. survive (43), but also where salt-scaling effects start to destroy solid materials like concrete or rocks (44).

In order to investigate the concentration and distribution of impurities in various ice samples ranging from hail stones (45; 46; 47; 48) microscopical as well as laser light scattering techniques have been employed to glacial ice

cores (49). Prodi (50), for example, measured the local density difference based on X-ray adsorption in hail stones to deduce the history of the ice particles. But these techniques did not provide any 3D-information of the trapped voids and precipitates. Only zones of higher as well as lower inclusion density were found. Mader et al. (51) analyzed the size of triple junctions on a more microscopical level using a regular microscope. Besides this classical approach, the geometrical studies on impurities in ice published so far employed electron microscopy (52). Barnes et al. (53; 54) used this method to analyze several ice core samples after evaporative etching of the upper few micrometers. In this way they increased the local concentration of impurities and widened the cutting edges of grain boundaries with the surface of the sample. Mulvaney et al. (55) micro-spectroscopically characterized sulfur bearing components in triple junctions between ice crystals from ice cores using an electron micro-probe. Similarly, the speciation of various elements in triple junctions of glacial samples was elucidated based on Raman spectroscopy (56; 57).

Besides, textural data provide various information on the formation of the sample (58; 59; 60; 61). Such data are urgently required by atmospheric modeling studies (62; 63; 64; 65; 66; 67). Various approaches to deduce the growth and nucleation regimes exist based on geometrical data obtained via traditional light-microscopy (58; 68; 59; 60; 69). However, these 2D-imaging techniques cannot constrain higher-order geometrical attributes such as the connectivity of the pore-network. X-ray microtomography (XMT) overcomes this problem by providing non-destructive cross-sectional as well as 3D object representations from X-ray attenuation mapping. Here, tomography offers the possibility to determine the internal surface area and the individual volume of each inclusion. Both pieces of information are necessary to characterize the morphology of the voids inside the sample as well as its porosity.

Schneebeli and Sokratov (70) performed micro-tomography on snow using a bench-top tomography device located in a 'walk-in' cold room. X-ray

radiation was generated using Electron-Bremsstrahlung, which allowed a spatial resolution of 36.3 $\mu$m per voxel and provided a relatively large field of view of several square centimeters. Also synchrotron micro-tomography (SRXT) was previously extended to frozen samples like snow (71; 72; 73), with a spatial resolution of 5 $\mu$m. However, a factor of 3.5 higher resolution is necessary to detect micrometer-sized inclusions of gaseous or non-volatile substances. Furthermore, measurement times of several hours for a full scan were still needed preventing the study of dynamic processes on a micrometer scale.

Within this thesis a new setup for cryo-tomography has been developed. It was initially designed for the tomography end-station of the material science beam line at the Swiss Light Source (SLS, Paul Scherrer Insitut, Villigen, Switzerland) and allows to scan 1 $mm^3$ sized ice samples at temperatures ranging from 220 K to 270 K at high thermal accuracy. Additionally, it is highly portable to any other tomographic station. A single scan can be performed within 90 minutes, which provided the basis for first steps towards time-resolved tomography experiments.

Hence, in order to assess the chemical activity of such multi-phase systems like natural ice, it is of interest to study how different impurities and physical conditions influence the morphology of the resulting inclusions and to what extend the initially trapped voids reshape due to temperature changes for example. Knowing these characteristics the transport- and reaction capacities of atmospheric ice particles can be estimated. Therefore naturally occurring ice particles as well as artificial samples were analyzed not only to experience the limits of this experimental setup but also to characterize inclusions trapped under various conditions geometrically. The interaction of aerosol proxies as well as a possible dependence of void morphology on temperature were elucidated in subsequent experiments. The results from examining such artificial samples were compared to natural specimen. Additionally, 'pseudo' 4D-experiments gave a first glance at how inclusions may metamorphose and how they may get transported within

an ice particle. The obtained data set forms a basis to improve estimates of the chemical potential of atmospheric ice particles with respect to the surrounding gas phase as well as estimates of their physical and mechanical properties.

# 2 Methods

## 2.1 Particle sampling and preparation

### 2.1.1 Natural samples

Natural samples were collected at the university campus at Mainz on $30^{th}$ March 2005. An open dewar vessel filled with liquid nitrogen was exposed to the precipitation. With a black tissue next to the dewar it was monitored if snow already reached the vessel. As soon as more snow than hail started to fall into the dewar, it was sealed immediately. The dewar was stored in a refrigerator at 240 K until all liquid nitrogen had evaporated. Afterwards the snowflakes were manually removed from the sampled particles in a cold room. Single grains were sealed airtight in plastic vials (Zinsser Analytics) and stored for 14 days until analysis at a temperature of 240 K in order to reduce reshaping due to metamorphism (70; 72; 73; 74; 75; 76; 77). Based on their shape and density the sampled particles were classified as hail stones (17).

Additionally, natural ice particles were collected at the Jungfraujoch (Switzerland) in March 2006 during the CLACE 5 campaign. Similarly to the just described procedure, a dewar, partly filled with liquid nitrogen, was placed on one of the terraces of the research-station shortly before a precipitation event. In contrast to the sampling procedure at Mainz, it could not be monitored which kinds of ice particles entered the vessel. After the precipitation event the dewar was placed in a refrigerator (240 K) until all liquid nitrogen had evaporated and the remaining ice particles were stored in Zinsser vessels. These were transported to Mainz in a well isolated and electrically cooled box at a temperature of 240 K. After their arrival, the containers were brought into a cold room, where snow flakes were removed manually. Until the experimental shifts at the SLS these samples were stored in liquid nitrogen. For the 400 km long transport to SLS the Zinsser vessels were placed in a $LN_2$ dewar filled with fine grained dry ice.

The dry ice was additionally sintered using liquid nitrogen once all samples were inside this transport-unit.

### 2.1.2 Sodium bromide doped ice samples

**Sodium bromide doped ice samples for the metamorphism experiment** A sodium bromide solution ($10^{-4}$ molar, analytical grade NaBr, VWR) was prepared using pure MilliQ water (resistivity 0.0055 $\mu$S). A solution droplet of a volume equivalent to 2 $\mu$L was brought into a polyamide sample-tube using a 10 $\mu$L syringe, which was pre-filled with cycloheptane. This organic matrix completely embedded the water droplet and fixed it mechanically (once the cycloheptane was solid, $T_{melting}$ = 260 K) when it was cooled down from room temperature (295 K) to the experimental temperature (230 K) and also during its freezing process. Since the organic solvent is hydrophobic, but wetted the surface of polyamide, the water droplet was forced to stay in spherical shape in the center of the sample holder during freezing.

The metamorphism experiment was conducted as follows: After the first tomographic run at 230 K the experimental temperature was set to 250 K. Once this temperature was reached, the sample equilibrated for half an hour. Then a second scan was performed and afterwards the experimental temperature was set to 230 K. After 30 minutes of equilibration at the lower temperature, the last scan was performed. These three scans will be called steps 1 to 3. A temperature profile of the experiment as well as three-dimensional reconstructions of air- and NaBr-filled inclusions are presented in Figure 5 and 6.

**Sodium bromide doped samples frozen at various exposure temperatures** For the second experiment, droplets of the same salt solution (0.2 $\mu$L, dosed with a 10$\mu$L syringe) were placed on a paraffin support to mimic atmospheric conditions. Then these paraffin blocks were brought into cold rooms having a temperature between 271 K - 200 K and stayed in these environ-

ments for at least 12 h to ensure freezing of the droplets. Samples frozen at 271 K, 263 K and 261 K were prepared using a Lauda RC 6 cryostat while the 243 K ice particles were manufactured in a Foron 4star refrigerator. A cold room at 203 K was generated by manually mixing tri(propylene-glycol)butyl-ether (Sigma Aldrich, analytical grade) with liquid nitrogen within a dewar. Once the organic matrix was solid ($T_{melting}$ = 200 K) two PT-100 elements were place inside the dewar. The first one layed on top of the solid ether close to the paraffin substrate while the second one was place 2 cm above the droplets. The temperature was constantly monitored and did not exceed 215 K within 12 h. After that period of time the frozen droplets were gently removed with a nitrogen cooled spatula. Since none of the solutions had been degassed a priori, multi-phase systems consisting of air, ice and brine were formed. A detailed description of the sample preparation is also provided in the literature (78).

Ice nucleates from this solution at supercooled temperatures comparable those ones needed to nucleate ice from pure water (79). Pruppacher (80; 81) showed that the growth rate of ice strongly depends on the degree of undercooling as well as on the concentration of the solution. A $10^{-4}$ molar concentration of NaBr should only slightly decrease the growth rate of the ice crystals (80).

### 2.1.3 Multi-phase systems

For the third experiment mixtures of common aerosol proxy substances (organics, NaBr, and mineral dust) were mixed with MilliQ water (resistivity 0.00055 $\mu$S). The sodium bromide, quartz, bentonite, and octanol were of analytical grade (Sigma Aldrich). Emulsions of octanol with pure MilliQ-water or octanol with a 1 wt.% NaBr solution were prepared by filling half a vial with the organic solvent and the other half with the aqueous solution. Suspensions were made from quartz and bentonite (clay) particles (size range 200 nm to 20 $\mu$m, 1 g mixed with 100 mL water) to simulate mineral dust components. The "mixed-mode-aerosol" suspensions were

generated by adding the minerals or the octanol to the NaBr solution. All these formulations were shaken in a vial with some head space at 400 rpm for 24 hours prior to freezing. Thereby equilibration with respect to air and octanol was reached.

Finally, fine droplets of these mixtures (0.2 $\mu$L) were placed on a hydrophobic paraffin substrate using a 10 $\mu$L syringe and immediately exposed to 240 K in a refrigerator. 12 hours later, the frozen droplets were gently removed from the paraffin surface using a spatula that had been kept in the refrigerator all the time, and sealed airtight in plastic vials (Zinsser Analytics). A detailed description of the sample preparation is also provided in the literature (82).

## 2.2 Cryotomography setup

### 2.2.1 Micro-tomography setup

Micro-tomography was performed at the tomography end-station of the materials science beam line at the Swiss Light Source (SLS) of the Paul-Scherrer-Institute at Villigen, Switzerland. Only a short summary of the principle of operation will be given here, as the setup for tomography is described elsewhere (83).

The monochromatic X-ray beam ($\Delta$E/E = 0.014%) was confined to a profile of 1.4 mm$^2$ to limit irradiation to the scanned region of interest (ROI). The beam energy was set to 13.5 keV, which is slightly higher than the K-edge of Bromine and therefore maximizes the X-ray adsorption contrast between the ice and the salt. This energy also provided enough flux to penetrate large samples. For the hail stones, which do not contain any contrast medium like NaBr in appreciable concentration, the energy was reduced to 10 keV in order to increase the contrast between the ice and its surrounding matrix of cycloheptane. Once the X-rays had passed the sample, they were converted into visible light by a thin Ce-doped YAG scintillator screen (Crismatec Saint Gobain, Nemours, France). The re-

sulting projection images were magnified with a standard microscope and photographed by a high-resolution CCD-camera (Photonic, Science, Ltd., East Sussex, UK). The optical magnification was set to 20x and 2x hardware binned to improve the signal-to-noise ratio. Thus isotropic voxels of 1.4 microns were obtained for the reconstructed images. In each measurement, 1001 projections were acquired with periodic dark and flat field images at an integration time of 2s each. Thus, within 90 minutes a sub-mm sized particle could be scanned completely and resulted in 4 GB of projection data. These data were post-processed and rearranged online into flat field corrected sinograms on a 16-node Linux PC farm (Pentium 4, 2.8 GHz, 512 MB RAM) using highly optimized filtered back-projection routines (84; 85). The reconstruction of the ROI took less than 20 minutes for a full dataset.

The different phases (solid, liquid, gaseous) coexisting inside the sample were color coded with respect to their relative X-ray absorption intensities (CT-number). Thereby a strongly absorbing component appears in a lighter color (higher CT-number). The data sets of up to hundreds of GB in total obtained in this process were stored on portable hard discs for subsequent detailed image analysis.

#### 2.2.2 Sample holder

The sample holder was custom-made of a polyamide tube that could be closed air-tight with a polyamide cover bearing a metal tip (Figure 1) for centering the specimen to the rotational axis. The sample chamber was surrounded by 2 mm thick walls and had a concave drilled bottom to simplify the positioning of the ice particle on the rotational axis of the whole device. A few tenths of a millimeter below the sample chamber, a PT-100 resistor element (2 x 2.3 x 0.9 mm, Greisinger Electronics) was placed to record the actual temperature. These measurements lasted 0.2 seconds and were taken once per second to minimize heating of the sample by the PT-100 element. The accuracy of the sensor was specified as $\pm$ 1

°C by Greisinger Electronics. The complete sample holder (Figure 1) was placed into the standard mount at the beam line.

#### 2.2.3 Cooling of the sample holder

A flow of cold nitrogen gas was taken from the standard nozzle of a CryojetXL (Oxford Instruments) directed at the top of the sample holder to cool the sample. A cage of two concentric Kapton-tubes was mounted airtight on the cryojet nozzle (Figure 1). These tubes were kept at a constant distance to each other by two aluminum rings located at the top and bottom of the cage.

The cryojet provides two concentric gas flows (Figure 1). Both were directed into the inner part of the Kapton-cage. The outer gas low (2 L/min) was designed to protect the cryojet from icing due to water condensation inside the nozzle as well as to avoid any ice formation or condensation on the sample in conventional use during protein crystallography. It will be called shield-flow in subsequent parts. The inner cold gas flow (10 L/min, ca. 210 K and 8 mm in diameter) could be temperature controlled in steps of 0.1 K as specified by Oxford Instruments, while the outer one was at room temperature (10 mm in diameter, about 295 K). By changing the mixing ratio of both flows, fast and well defined changes of the sample's temperature could be achieved. This feature was needed to reduce temperature fluctuations while taking reference images, when the sample holder was moved out of the beam toward the warmer walls. The total outflow of nitrogen (12 L/min) was strong enough to prevent any circulation of ambient humid air from the hutch into the cage, even when turbulent mixing occurred due the presence and movements of the sample holder. Hence, no icing or condensation inside the cage or on the polyamide-cup occurred during the experiments.

The space between the two concentric Kapton-tubes was additionally flushed with dry nitrogen (298 K, quality grade 5.0, approx. 0.9 L/min.) from a bottle. The gas escaped via two small holes at the bottom between the

two foils. Thus, no condensation of ambient humidity could occur on the Kapton-foils, which served as a window for the X-ray beam. Such condensation in the optical path during the experiments would have significantly biased the resulting reconstructions.

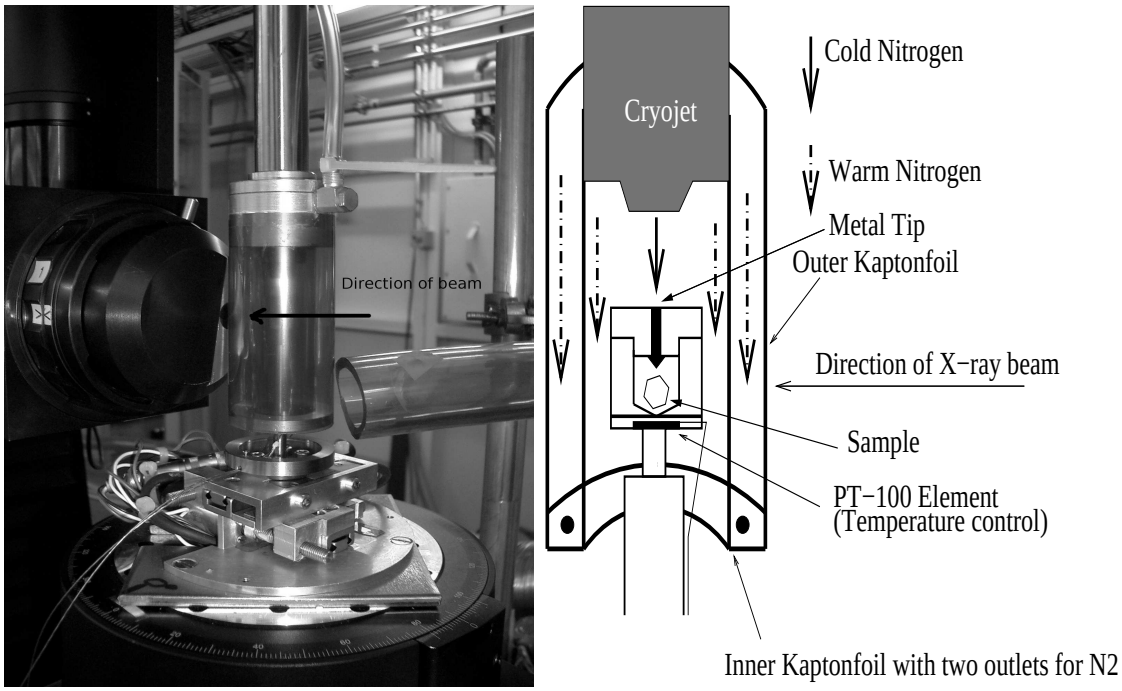


Figure 1: Photograph and schematic drawing of the setup at the SLS.
In the left picture the setup at the tomography end-station is presented. The camera is slightly moved out of position and an additional tube was added to suck the cold gas-flow away from the micro-mechanics. The schematic drawing on the right side depicts the different parts of the setup, which are hidden in the photograph on the right side.

### 2.2.4 Sample mounting

At all times, the samples and the tools required for sample handling and mounting were kept inside an isolated box filled with dry ice for temperature preconditioning (T = $\sim$ 200 K). Directly before the scan, the ice particle was placed in the polyamide sample holder. Unless specified otherwise, all samples were embedded in freshly molten cycloheptane. To ensure the cooling of the sample holder during its transport from the dry ice box to the goniometer stage, each fully loaded polyamide cup was embedded into a bag filled with crushed dry ice. Before the sample holder

was tied to the standard sample mount of the beam line, the Kapton-cage was slid up and the cold gas flow of the cryojet was turned to its maximal strength of 10 L/min. Additionally, the shield flow was shut off. After fixing the sample holder onto the sample mount, the dry ice bag was removed. Nearly at the same time, the Kapton-cage was slid down again to ensure continuous cooling of the sample. Then, the cryojet was centered on the rotational axis of the sample holder. The sample adjustment was fine-tuned with respect to the beam line optics using the metal tip located in the head of the polyamide tube. Finally, the position of the cryojet was readjusted to the rotational axis of the sample holder. This fine-tuning was completed when no temperature fluctuation was detectable any more during a 180 degree rotation of the sample holder.

### 2.3 Raw data processing

Depending on the stability of the synchrotron beam some samples required additional filtering using an 'edge preserved smoothing' filter provided by AMIRA (Mercury Systems). This algorithm uses a small kernel (size: 3x3) and works similarly to a Gaussian filter (85). Well known smear-out effects were significantly reduced by the edge-sensitivity of this algorithm which stopped the filtering-process in the vicinity of an edge-detection.
The different types of inclusions (salt, air, organics, mineral dust, etc.) and ice were segmented based on threshold values. The CT-numbers (relative X-ray adsorption) for salts ranged from 0 to 10 and for air from 245 - 255, if not specified otherwise. Ice was assigned a threshold of 40 to 120. A combination of the *"burning algorithm"* (86) and subsequent triangulation [1] were used to identify individual and to gain the following geometrical characteristics:

1. surface area of each pore: $A_i$
2. volume of each pore: $V_i$

[1] See appendix for comments on these algorithms.

3. surface area of all pores: A

4. volume of all pores: V

The latter two values were required since the burning algorithm in AMIRA uses a byte-based matrix to record the individual voids. Such an implementation is limited to a maximum of 255 objects. Therefore threshold values for the size of the voids were used to gain groups of inclusions with less than 255 members. Only in a few extreme cases this was not possible. These samples were cut into stacks of 50 to 100 slices. Unless otherwise specified, the reported data refer to the whole sample and no cutting was required.

## 2.4 Geometrical characterization

### 2.4.1 Sphericity ($\Psi$), volume-to-surface ratio and porosity

In the analyzed multi-phase systems inclusions of various shapes were found. Their sphericity (87) was calculated according to the following formula describing the trapped inclusions in terms of their similarity to a sphere:

$$\Psi_i \equiv \frac{\pi^{\frac{1}{3}} \times (6V_i)^{\frac{2}{3}}}{A_i} \tag{1}$$

All voids were further separated in bins describing their morphology as small or large cylinders, small or large threads as well as as elongated or very elongated objects based on their decrease of $\Psi_i$ respectively. Therefore the above formula was applied to an ellipsoidal volume (87):

$$\Psi \equiv \frac{2(ab^2)^{\frac{1}{3}}}{a + \frac{b^2}{\sqrt{a^2+b^2}} ln(\frac{a+\sqrt{a^2-b^2}}{b})} \tag{2}$$

where $a$ and $b$ are the main axes of the ellipsoidal object and their ratio was varied as follows:

- Small cylinders = 1:10
- Large cylinders = 1:20
- Small threads = 1:40
- Large threads = 1:50
- Elongated objects = 1:60
- Very elongated objects = 1:80

The volume-to-surface ratio (88) was calculated as $V_i/A_i$. As pointed out by Lowell et al. (89), this ratio is commonly used to correlate pore-size and geometry with the adsorption of different gases onto the internal surface of porous media (BET, Porosometry).
The porosity of a sample was defined as the ratio of volume filled by air over the total volume of the specimen.

#### 2.4.2 Crystal size distribution analysis (CSD)

Crystal size distribution analysis (CSD) was developed by Randolph and Larson (61). Marsh (58) introduced it as a petrological method in 1988 and subsequently extended it to the analysis of the textural evolution of various samples (59; 60; 68). As these studies were mainly based on optical microscopy, CSD was initially developed using the length of crystals as raw data. Higher order geometrical characteristics, like the surface area or the volume of the individual voids could only be calculated as higher order moments of the size distribution involving shape factors and stereographic corrections (90).
Tomography, as an analytical technique, overcomes these limitations. Instead of the length of the individual objects, their volume and surface area were obtained from the analysis of the experimental data. Especially the volume, which is proportional to the length of the analyzed object, was used in the following.

CSD is based on the crystal population-density (61). This density has been expressed in various ways, like for example as the derivative of a cumulative distribution with respect to bin size. In this study, the definition of Marsh (58) was employed, but was modified using the volume of the voids instead of their lengths. The population-density n($V_i$) is the number of inclusions in any size range (bin) divided by the size range and normalized to a volume of unity. The volume of unity was chosen to be 1 mm$^3$ since the sample volume varied from 0.7 to 0.9 mm$^3$. n(V) can mathematically be expressed as:

$$n(V) \equiv \frac{dN(V)}{d(V)} \tag{3}$$

where N(V) is the total number of voids in a certain size range d(V). Furthermore n$^\circ$ shall be defined as:

$$n^\circ \equiv \frac{dN(V)}{d(V)}|_{V=0} \tag{4}$$

n$^\circ$ was obtained by fitting the population density and extrapolating it to zero.

From the population-density plots (ln(n) versus V, like in figure 7 by Marsh (58)) the dominant growth-regime during the solidification of the sample can be deduced. In this study (Figures 10 and 13) the resulting curves are convex downward like for most natural samples (cf. Figure 9 by Marsh (58), Figure 7 by Cashman et al. (68), etc.). This shape indicates that a certain degree of accumulation occurred during solidification. Using the scaling law relationships derived by Brandeis et al. (91) as well as the approach of Zieg and Marsh (59) one can obtain an approximate growth rate of each individual inclusion $G_i^{approx}$ as well as an approximate nucleation rate $J_i^{approx}$ based on the following mathematical relations:

$$G_i^{approx} \equiv \frac{c_1}{S_i \tau} \tag{5}$$

$$J_i^{approx} \equiv \frac{c_2 \times n^\circ}{S_i \tau} \tag{6}$$

where $S_i$ is the absolute value of the slope of the population density at the Volume i
($S = |n'(V_i)|$). This value was determined by linearly fitting the curves in Figures 10 and 13 and calculating the first derivative of the resulting functions. Brandeis et al. (91) as well as Zieg and Marsh (59) showed that the constants $c_1$ and $c_2$ are close to unity and can be neglected once the residence time ($\tau$) of a crystal in the liquid phase can be assumed to be equal to the time required for complete solidification of the sample ($\Delta$t). In this study, this assumption could be made, because ice crystal growth rates of several millimeter to centimeter per second can be expected (80; 81) under the actual experimental conditions. In order to calculate $\Delta t$, the approach by Pruppacher and Klett (17, Chapter 16) determining the freezing time of an aqueous droplet in the atmosphere was used. Clearly, this approach only provides estimates of the growth and nucleation rate. Therefore, to avoid confusion with the real growth and nucleation rate which may be calculated using models of higher complexity like molecular dynamics. The terms 'approximate nucleation' and 'approximate growth rate' will be used in the following also because these values were derived from a fit of the population density and an empirical fit of $\Delta t$ (17). However, comparing the results obtained in this study with the experimental values for the growth rate of ice from salt solutions (80), good agreement has been achieved.
Finally, plotting the logarithmic population-density ($\ln(n^\circ)$ versus the absolute value of it's slope S (Figure 14)) allows the first interpretation of the relative differences in solidification process (59). The higher both values get the faster the sample solidified.

# 3 Results

## 3.1 Hail Stones and naturally occurring ice particles

### 3.1.1 Hail stones collected at Mainz

Two hail stones were collected on the Campus of the University at Mainz and analyzed at the SLS. Thereby the energy of the beam was reduced to 10 keV to increase the adsorption contrast between the ice and possible impurities inside the sample as well as the contrast between the ice and cycloheptane. One of the samples (hail stone 1) was placed inside the polyamide cup without the embedding organic matrix (74). This hail stone showed air bubbles of an unique morphology, as all its inclusions were Y shaped (Figure 2). Unfortunately, the exact conditions of formation of this grain are unknown and consequently the reason for this pore geometry cannot be explained. An onion-like layering of air-filled voids was found similar to earlier studies on hail stones and atmospheric ice particles (17; 45; 46; 47; 48; 92; 93).

The average volume occupied by air was $3.58 \times 10^{-16}$ m$^3$ with an average surface area of $4.88 \times 10^{-10}$ m$^2$. Besides an average volume-to-surface ratio of 0.95 $\mu$m and an average sphericity of 0.53 were determined. Furthermore, one part of the grain was just pure ice, without any inclusions. Such a particle may form due to a collision and subsequent freezing of two ice particles inside the dewar used for sampling.

The second hail stone (hail stone 2) was embedded in freshly molten cycloheptane ($T_{melting}$ = 260 K). It exclusively exhibited spherical pores with an average volume of $3.70 \times 10^{-16}$ m$^3$ and an average surface of $3.96 \times 10^{-10}$ m$^2$. The average volume-to-surface ratio reached 1.33 and an average sphericity of 0.75 reflected a high amount of well rounded pores.

This shape variation from Y-shaped to spherical may be natural, since preparation and experimental conditions were identical for both samples. The limited number of samples did neither allow to rule out different conditions of formation (for example: higher temperatures) nor longer atmo-

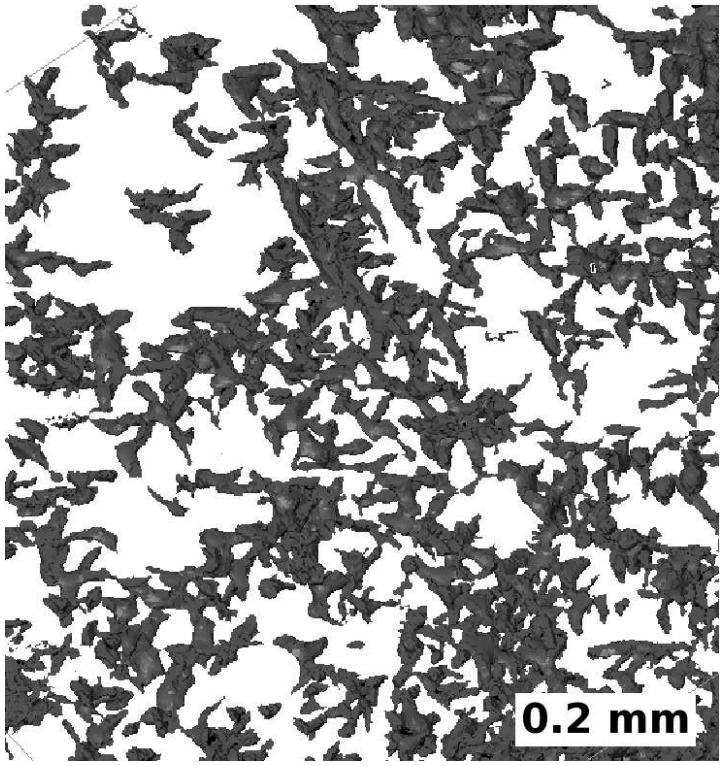


Figure 2: Unmetamorphosed Y-shaped inclusions of air.
The onion-like layering of these pores can be estimated from this picture.

spheric residence times in reservoirs of warmer air before sampling. Geometrical characteristics like the porosity and surface area of the hail stones are compiled in Table 1.

No further impurities apart from air were found inside the grains. Ionic substances, if present, may have been of such a low concentration that no significant adsorption contrast could be reached. Solid particles, like mineral dust, known to act as ice nuclei, were completely absent in these two samples or smaller than the voxel resolution of 1.4 $\mu$m.

Table 1: Geometric characteristics of the natural samples.
The porosity is reported as the ratio of the volume occupied by gases over the total volume of the sample. Average volume and surface area were calculated as the ratio of total volume / surface area divided by the number of identified pores, while the sphericity and the volume-to-surface ratio are reported as average values ( ± standard deviation) derived for each pore individually.

| | Hail stone 1 | Hail stone 1c | Hail stone 2 | Jungfraujoch 1 | Jungfraujoch 2 |
|---|---|---|---|---|---|
| Grain | | | | | |
| Surface [$10^{-6}$ m$^2$] | 1.49 | 0.37 | 7.44 | 2.02 | 2.92 |
| Volume [$10^{-10}$ m$^3$] | 2.65 | 2.66 | 3.38 | 1.52 | 1.65 |
| Pores filled with air | | | | | |
| Surface [$10^{-7}$ m$^2$] | 4.83 | 2.79 | 0.59 | 2.26 | 4.51 |
| Average surface area [$10^{-10}m^2$] | 4.87 | 4.10 | 3.90 | 30.23 | 26.5 |
| Volume [$10^{-13}$ m$^3$] | 3.54 | 2.36 | 0.56 | 6.9 | 8.03 |
| Average volume [$10^{-16}m^3$] | 3.55 | 3.47 | 3.71 | 93.11 | 47.22 |
| Number of pores | 987 | 680 | 151 | 75 | 170 |
| Sphericity | 0.53 | 0.63 | 0.75 | 0.43 | 0.55 |
| Standard Dev. | 0.14 | 0.16 | 0.17 | 0.12 | 0.18 |
| Volume/Surface [$\mu$m] | 0.95 | 1.18 | 1.32 | 1.05 | 1.33 |
| Standard Dev. | 0.3 | 0.38 | 0.29 | 0.36 | 0.7 |
| Porosity [%] | 0.13 | 0.08 | 0.02 | 0.46 | 0.49 |
| Inner-to-outer surface | 0.32 | 0.75 | 0.01 | 0.11 | 0.15 |

**Metamorphosis induced by heating** The metamorphism of ice was the target of various studies. Apart from isothermal (76; 77; 94) also temperature-gradient driven metamorphism was investigated (70; 72; 73). The theoretical background was elucidated by Saunders et al. (95; 96; 97) and Colbeck (75; 98; 99). All these studies focussed on the shape changes that occur to snow crystals and neither atmospheric ice particles, nor their internal structure were investigated.

Apart from using different driving forces for the metamorphism, the above mentioned studies agree that the specific surface area of snow shrinks as metamorphism progresses. Also the curvature of the exposed surfaces decreased (76). Dominé et al. (76) reported in great detail to what extend surface features are lost during this process of recrystallization.

In order to follow the metamorphism of the Y-shaped pores inside of hail stone 1, the first tomographic scan was performed at 230 K (hail stone No. 1). Then the temperature to 260 K was risen, where the sample equilibrated for half an hour. After this time a second scan was performed (hail stone No. 1c).

From the different scans it became obvious that the shape of the air-filled inclusions changed drastically during heating. All originally Y-shaped pores became spherical (Figures 2 and 3), which was reflected by an increase in sphericity and in volume-to-surface ratio. In addition, a reduction in the mean pore-size was traced, indicating that some air either left the sample during heating or got trapped in inclusions smaller than the minimum spatial resolution. The porosity of the samples was already very low at the beginning of the experiment (0.13%), and decreased (0.08%) during heating, (Table 1). The total number of pores decreased from 987 to 680, whereas the average surface area shrank only slightly during the experiment and the average pore volume stayed approximately constant. This indicated, that the larger inclusions must have decomposed into ones smaller than the minimum spatial resolution.

Dominé et al. (76) already discussed the decrease of surface area during

isothermal as well as temperature-gradient driven metamorphism for snow samples. In comparison with other studies (70; 72; 73; 76; 77; 94) it became evident that shape metamorphism should always lead to a minimization of specific surface area. Regarding the surface of hail stone 1 these findings could be reproduced (Figure 3). This experiment extended previous studies to the interior of naturally occurring ice particles as well as artificial samples.

Before metamorphism:

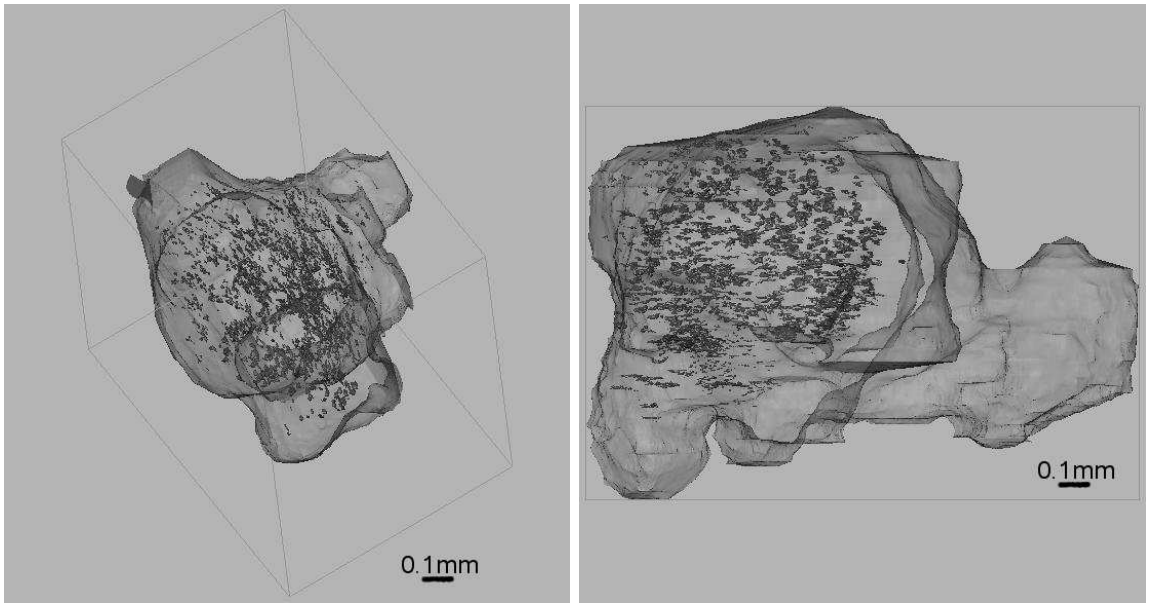


After metamorphism:

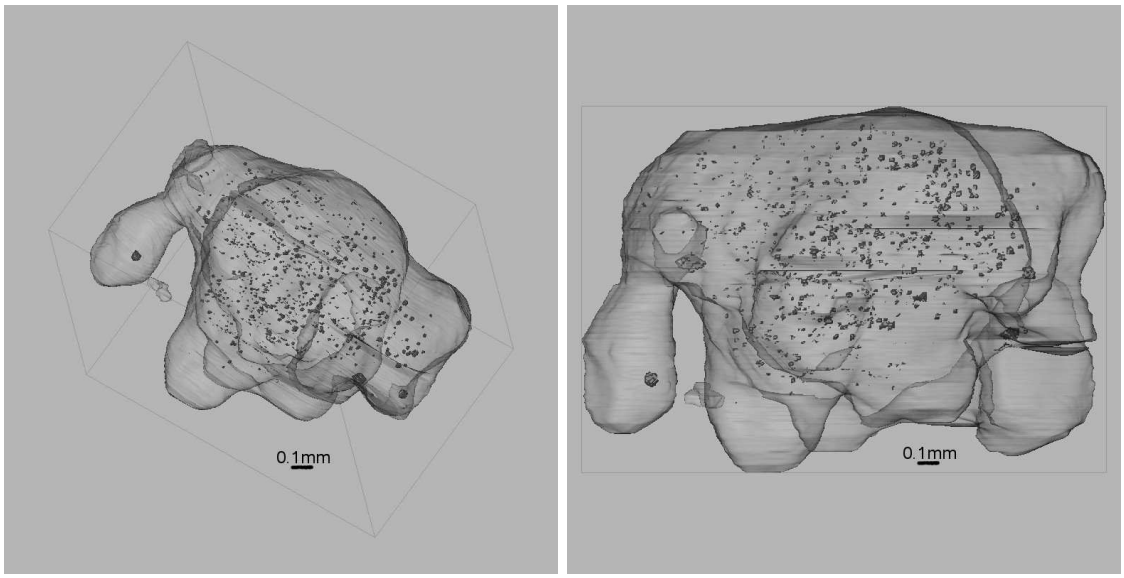


Figure 3: Outer surface and porosity of hail stone 1 before and after its forced metamorphosis.

### 3.1.2 Ice particles collected at the Jungfraujoch

Five particles were collected at the Junfraujoch and analyzed at the SLS. The energy of the X-ray beam was adjusted to 13.5 keV and the samples were not embedded in cycloheptane. Only in two samples air-filled voids could be found (Figure 4). These samples will be discussed further in the following. The remaining three were small dendrites and showed no inclusions. It was assumed that these samples consisted of pure ice.

The two particles bearing air-filled inclusions showed rather dendritic forms, but the degree of possible riming (collision with cloud droplets and subsequent freezing, (4; 17; 18)) could not clearly be determined. The air bubbles were distributed more or less homogeneously over the total volume of ice.

The voids in particle 1 exhibited an average volume of $9.31 \times 10^{-15}$ m$^3$ with an average surface area of $3.02 \times 10^{-9}$ m$^2$. A porosity of 0.46% and an average sphericity of 0.42 were calculated. The volume-to-surface ratio reached a value of 3.1 $\mu$m while the ratio of inner-to-outer-surface could be determined as 0.11%.

Particle 2 showed a slightly different shape. It is more condensed and compact compared to the rather fragile looking particle 1 (Figure 4). Like in the previous sample, the air bubbles were also homogeneously distributed and possessed an average volume of $4.72 \times 10^{-15}$m$^3$. Their average surface area was measured as $2.65 \times 10^{-9}$m$^2$. These voids had a sphericity of 0.55 with an average volume-to-surface ratio of 1.8 $\mu$m. The ratio of inner-to-outer-surface was determined as 0.15%. All geometrical characteristics of these particles are compiled in Table 1.

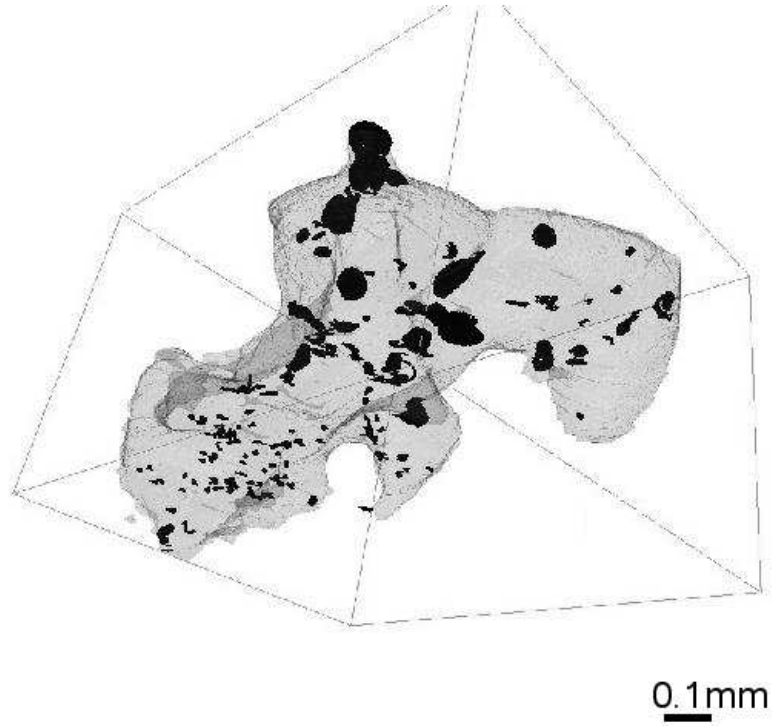


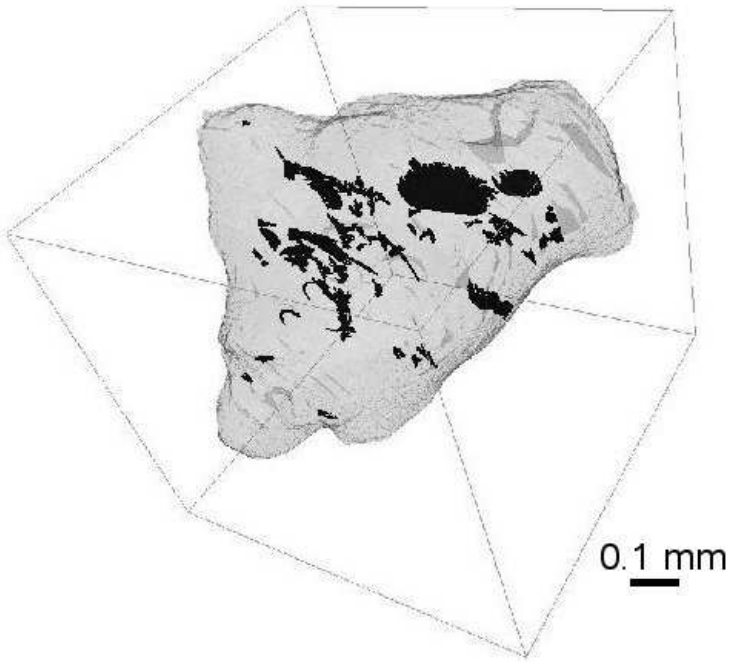


Figure 4: Two particles collected at the Jungfraujoch (Switzerland).
While the air is presented in black the ice appears as light grey. Note the completely different shapes and sizes of the pores.

## 3.2 Metamorphism of inclusions in a diluted ($10^{-4}$ molar), frozen NaBr solution

### 3.2.1 Morphology of air- and salt-filled inclusions

In Figures 5 and 6 (step 1, each) the air and salt inclusions are presented. Going from top to bottom within these images three different morphologies can be distinguished. On top, sheet like structures can be seen. These are flat and aligned parallel to each other. In the middle of the sample, they turn into channels. Such one-dimensional objects might be grain boundaries (or so-called veins, (51)). As one approaches the bottom of the scanned volume the amount of small spherical and ellipsoidal inclusions increases. Furthermore V-shaped bodies are identified. These can form at points, where three grain boundaries meet. Unfortunately, the orientation of the ice crystal could not be determined, which would have allowed the reconstruction of the vein network. The V-shaped inclusions resemble the shape of triple junctions found in ice at temperatures close to the melting point (51; 55). Nevertheless, similar results were obtained in sea-ice freezing experiments (8; 100).
The great lack of two or even three-phase inclusions in all samples, like air and salt or air, salt crystals and brine together in one void, suggests that the mechanism of trapping of NaBr and air are independent.

### 3.2.2 Metamorphism of air-filled inclusions

A three dimensional reconstruction of the air-filled inclusions is shown in Figure 5 (step 1). A section of 768 x 834 x 690 $\mu$m is presented at the three different steps of the temperature cycle (step 1: 230 K, step 2: 250 K, step 3: 230 K). The distribution of the air-filled pores underwent strong changes, as can be seen from the 3-dimensional reconstruction (Figure 5). The number of pores rose by an order of magnitude (from 423 to 4260, Table 2). The total volume of the air-filled voids decreased slightly (from 3.68 to $3.11 \times 10^{-11}$ m$^3$). Hence, the average pore volume shrank by about

an order of magnitude from $1230 \times 10^{-14}$ m$^3$ to $124 \times 10^{-14}$ m$^3$, whereas the average surface area in each individual pore decreased by about a factor of ten, indicating that elongated, rotational-symmetric and more or less ellipsoidal bodies transformed into small spheres. However, to gain these measurements the tomographic data had to be cut into stacks, which adds a maximum error of 15% to the reported values. The error was estimated by assuming a homogeneous distribution of pores over the stack and calculating the additionally created surface during the cutting process. The total amount of air trapped in ice ranged from 3.68 x $10^{-11}$ m$^3$ to 3.11 x $10^{-11}$ m$^3$ while moving from step 1 to step 3. The porosity of this specimen varied from 6.14% (step 1) to 5.19% (step 3).

During metamorphism the total surface of air filled voids stayed more or less constant, while their total volume decreased, which also indicates the formation of small spherical structures. This finding could as well be deduced regarding the change of the sphericity. The average of this factor nearly doubled, while the volume-to-surface ratio reached a final value of 2.6 $\mu$m.

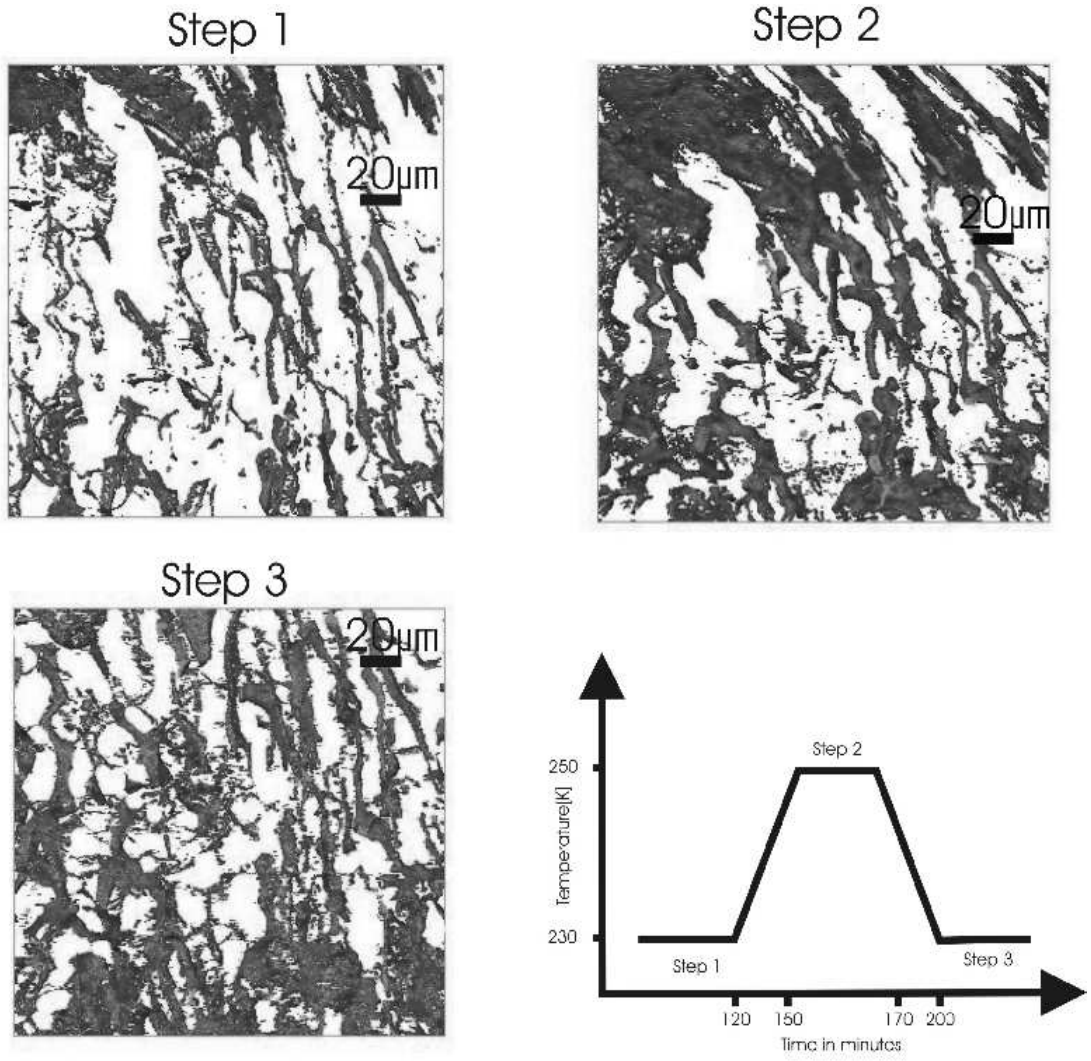


Figure 5: Air-filled inclusions in ice frozen from a $10^{-4}$ M NaBr solution and their response to controlled temperature changes.
In all 3 images, the same region (768 x 834 x 690 $\mu$m) was selected to present the changes occurring to air-filled pores, when the initial distribution in ice (top left) was heated to 250 K (top right) and re-equilibrated at 230 K (lower left). The lower right panel shows the applied temperature cycle.

### 3.2.3 Metamorphism of salt-filled inclusions

During the experiment, the total amount of NaBr in the region of interest grew from initially 1.01 $\times$ $10^{-14}$ $m^3$ to 284 $\times$ $10^{-14}$ $m^3$, the volume-to-surface ratio of the salt filled inclusions increased from 0.92 $\mu$m to 1.72 $\mu$m and the average surface area expanded from 1.01 $\times$ $10^{-9}$ $m^2$ to 12.2 $\times$ $10^{-9}$ $m^2$. Since the sphericity stayed more or less constant, it becomes evident that the overall shape of the trapped inclusions had not changed. A complete geometrical characterization of all the inclusions in the doped ice sample is presented in Table 2.

During the metamorphism large voids grew on the extent of smaller pores (Figure 6). The total amount of solid NaBr was recalculated by assuming that all precipitates were pure crystalline NaBr and had a density of 3.2 $g/cm^3$ (101). The trapped amount increased as metamorphism progressed (Table 2). This indicates an efficient transport of NaBr inside the ice sample. Since the major orientations of the resulting veins can be deduced in a vague way (Figure 6), brine transport predominantly along grain boundaries is suggested. Crystallographic information was not available but would be warranted to strengthen this hypothesis, e.g. by applying X-ray micro-diffraction experiments subsequently to tomography.

Table 2: Geometric characteristics of NaBr-filled inclusions in ice, frozen from a dilute NaBr solution ($10^{-4}$ moles/liter).
This sample was analyzed three times, first at a temperature of 230 K, then at 250 K, and finally again after cooling to 230 K. The porosity is reported as the ratio of the volume occupied by air over the total volume of the analysis. Average volume and surface were calculated as the ratio of total volume / surface over number of identified pores, while the sphericity and the volume-to-surface ratio are reported as average value ( $\pm$ standard deviation) of the data derived for each pore individually. The amount of NaBr in steps 1 and 3 was calculated assuming that the NaBr-filled inclusions had a density of 3.2 g/cm$^3$.

| | | Step 1 | Step 2 | Step 3 |
|---|---|---|---|---|
| Pores filled with air | | 240 K | 260 K | 240 K |
| Total surface | [$10^{-5}$ m$^2$] | 1.09 | 0.99 | 1.19 |
| Average surface | [$10^{-7}$ m$^2$] | 0.26 | 0.08 | 0.03 |
| Total volume | [$10^{-11}$ m$^3$] | 3.68 | 3.87 | 3.11 |
| Average volume | [$10^{-14}$ m$^3$] | 8.58 | 3.25 | 0.73 |
| Volume/Surface | [$\mu$m] | 1.53 $\pm$ 1.64 | 3.90 $\pm$ 1.23 | 2.60 $\pm$ 0.73 |
| Sphericity | | 0.36 $\pm$ 0.11 | 0.58 $\pm$ 0.15 | 0.58 $\pm$ 0.12 |
| Number of pores | | 423 | 1189 | 4260 |
| Pores filled with NaBr | | | | |
| Total surface | [$10^{-8}$ m$^2$] | 1.01 | 20.2 | 83.1 |
| Average surface | [$10^{-9}$ m$^2$] | 1.01 | 1.82 | 12.2 |
| Total volume | [$10^{-14}$ m$^3$] | 1.01 | 19.1 | 284 |
| Average volume | [$10^{-14}$ m$^3$] | 0.10 | 0.17 | 4.18 |
| Volume/Surface | [$\mu$m] | 0.93 $\pm$ 0.25 | 0.95 $\pm$ 0.20 | 1.72 $\pm$ 1.12 |
| Sphericity | | 0.45 $\pm$ 0.09 | 0.40 $\pm$ 0.09 | 0.46 $\pm$ 0.12 |
| Number of pores | | 10 | 111 | 68 |
| Volume of ice | | | | |
| Ice | [$10^{-10}$ m$^3$] | 5.99 | 5.98 | 5.97 |
| Weight of NaBr | [$10^{-6}$ g] | 0.03 | n.d. | 9.08 |
| Porosity | | | | |
| Porosity | [%] | 6.14 | 6.47 | 5.19 |

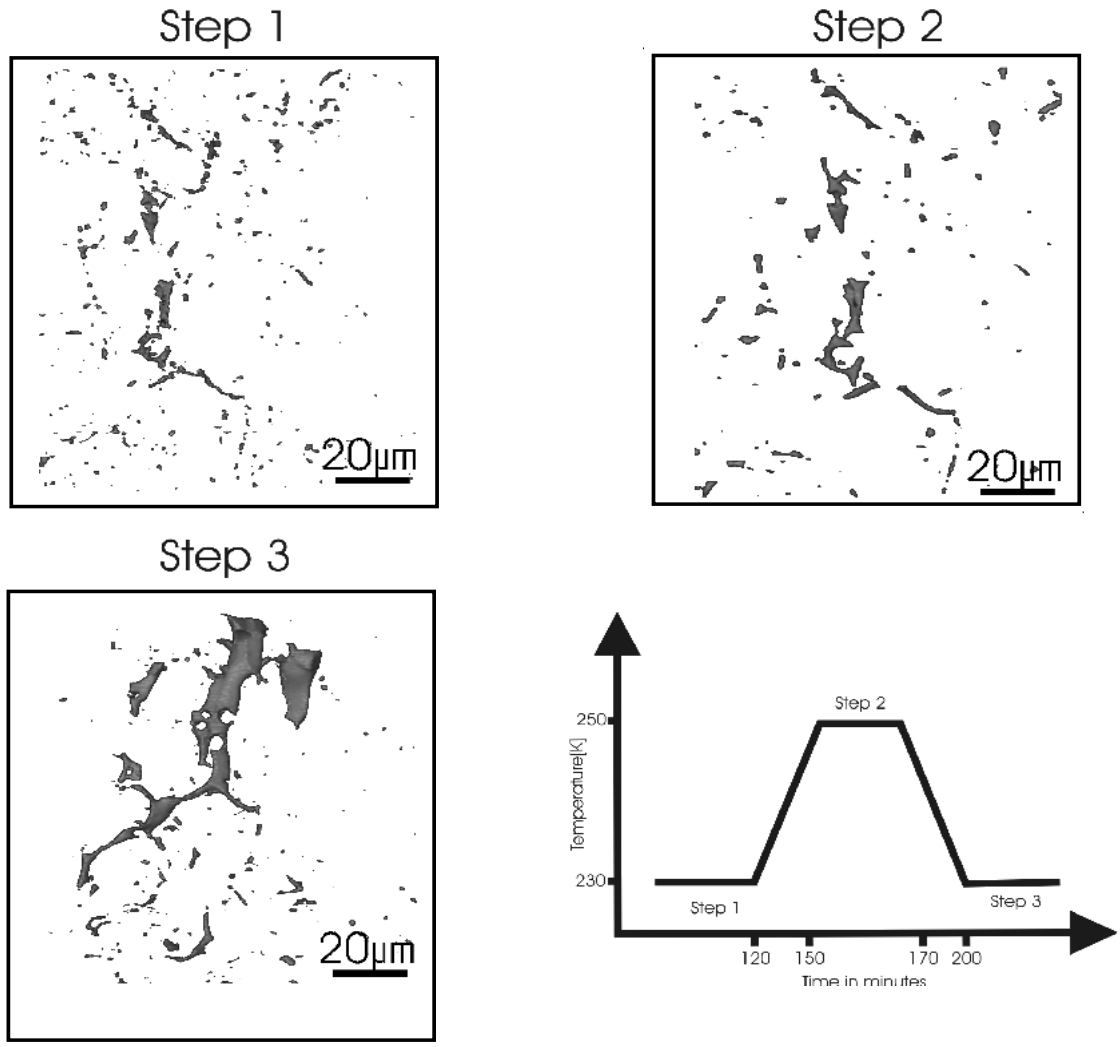


Figure 6: NaBr-filled inclusions in ice frozen from a $10^{-4}$ M NaBr solution and their response to controlled temperature changes.
In all 3 images, the same region (768 x 834 x 690 $\mu$m) was selected to present the changes occurring to NaBr-filled pores, when the initial distribution in ice (top left) was heated to 250 K (top right) and re-equilibrated at 230 K (lower left). The lower right panel shows the applied temperature cycle. Note the liquid phase is depicted in the upper right picture.

## 3.3 Temperature dependence of inclusion trapping in ice frozen from a $10^{-4}$ molar NaBr solution

Air- and salt-bearing inclusions were analyzed in samples frozen from a diluted (1 wt.%) NaBr solution on a paraffin substrate. These samples were exposed to temperatures from 271 to 203 K for freezing. A close-up photograph of a sample exposed to 200 K is presented in Figure 7. There, the NaBr precipitates appear in gold, while the air bubbles are colored in dark blue. Both types of inclusions are clearly visible and exhibit a distinct separation at all experimental temperatures. Their shapes and volumes are not homogeneous, as already mentioned by Carte (92), but a strong temperature dependence of their geometrical characteristics could be deduced (Figures 8 and 11).

At low under-cooling (263 K) small, more or less cubic to spherical inclusions filled by either air or salt were found. These were homogeneously distributed over the analyzed ice spheres. By either lowering the exposure temperature to 243 K and further or increasing it to 271 K, these voids grew into elongated bodies (Figures 9 and 12). The total number of threads and elongated objects increased and reached its maximum at an exposure temperature of approximately 243 K. In contrast to common expectancies the largest average volumes were found at very low temperatures (203 K) and at very high temperatures (271 K), as depicted in Figures 8 and 11.

It is suggested that the thread-like precipitates formed along grain boundaries, while the cubic and spherical inclusions are rather located in triple junctions (places where three grain boundaries meet). Rarely, plate-like objects, which indicate a position on crystal surfaces (plains), occurred.

In the following the characteristics of the NaBr- and the air-filled inclusions will be discussed separately.

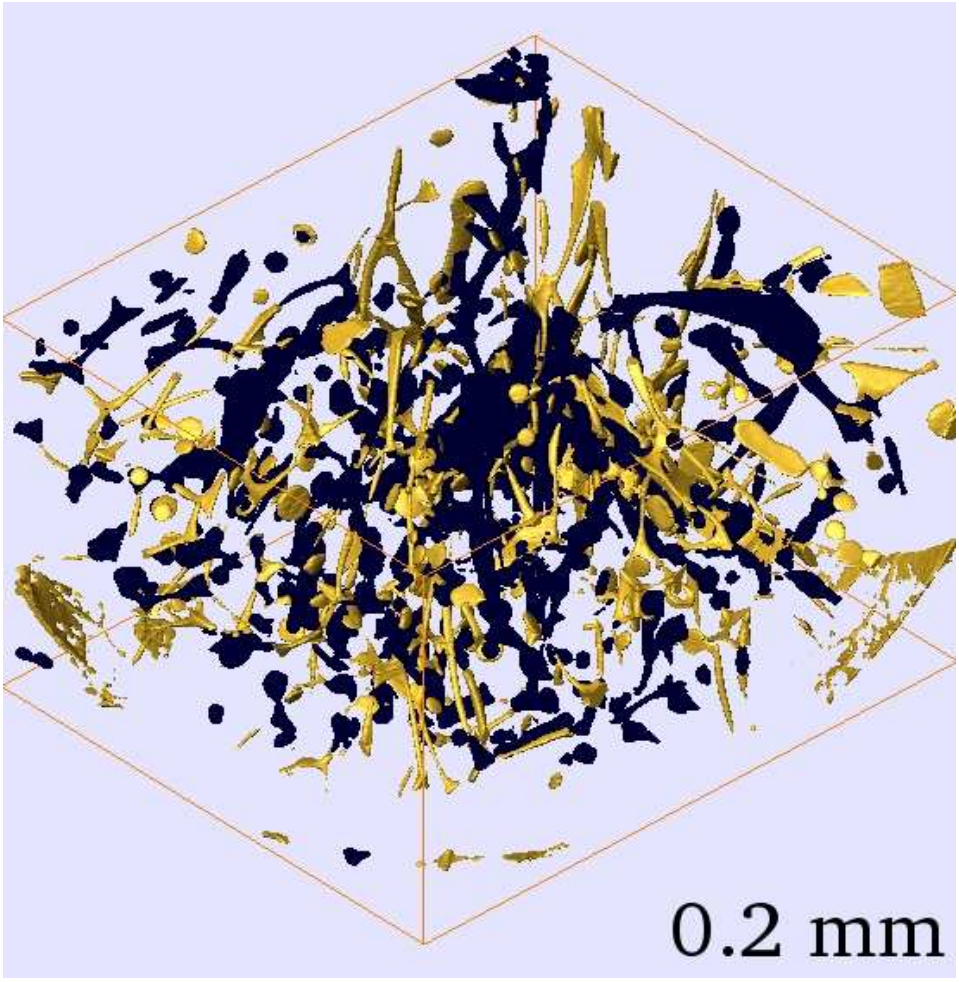


Figure 7: Close-up photograph of a $10^{-4}$ molar NaBr solution droplet exposed to 203 K for freezing.
Note that the NaBr-filled inclusions are colored in gold, while the air-filled inclusions appear dark blue. Two dominant geometries typical for both impurities: 1. threads and 2. flat disc-like inclusions. At higher exposure temperatures spherical voids will appear.

### 3.3.1 NaBr-filled inclusions

**Geometrical Characteristics of NaBr-filled inclusions** Figure 8 summarizes the geometric characteristics of the NaBr bearing inclusion. The NaBr precipitates exhibited an average surface area of $1.3 \times 10^{-8}$ m$^2$ at 271 K. This value decreased towards $0.9 \times 10^{-8}$ m$^2$ at 263 K and increased again as the exposure temperature approached 203 K. A similar behavior was found for the average volume of the voids. They exhibited a minimum of $0.8 \times 10^{-15}$ m$^3$ at 263 K and a maximum of $3.8 \times 10^{-15}$ m$^3$ at 203 K.
The sphericity, however, was lowest at the extreme points of the tempera-

ture interval investigated. At 271 and at 203 K elongated precipitates were dominant but they gradually transformed into smaller cubic voids as the exposure temperature in-/decreased towards 263 K. This finding is further supported by the volume-to-surface ratio which reached its maximum at an under-cooling of 10 K. The total number of NaBr-filled voids in the sample increased as the exposure temperature decreased (Table 3). In conclusions, the temperature dependence of average volume, surface area and sphericity can be expressed by the following empirical fits:

$$V_{average}\ [\mu m^3] = 47566.4 - 352.358 \times T + 0.66778 \times T^2 \quad (7)$$

$$A_{average}\ [\mu m^2] = 35557.6 - 249.474 \times T + 0.457218 \times T^2 \quad (8)$$

$$\Psi_{average} = -0.788505 + 0.0103335 \times T - 2.05349 \times 10^{-5} \times T^2 \quad (9)$$

where T is the exposure temperature in Kelvin. These empirical formulas have a $R^2$ index higher than 0.7 (Figure 8). The analysis of the pore-shapes was further extended by estimating the dominant pore-geometry with respect to temperature. To this end, the sphericity values ($\Psi_i$) were sorted in various bins to categorize the dominant pore-morphology as being either small or large cylinders, small or large threads, or elongated or very elongated objects. In Figure 9 the temperature dependence of the dominant pore geometry is presented. At the highest and the lowest exposure temperatures thin, but long precipitates were found. At moderate degrees of under-cooling spherical to cylindrical bodies were most common.

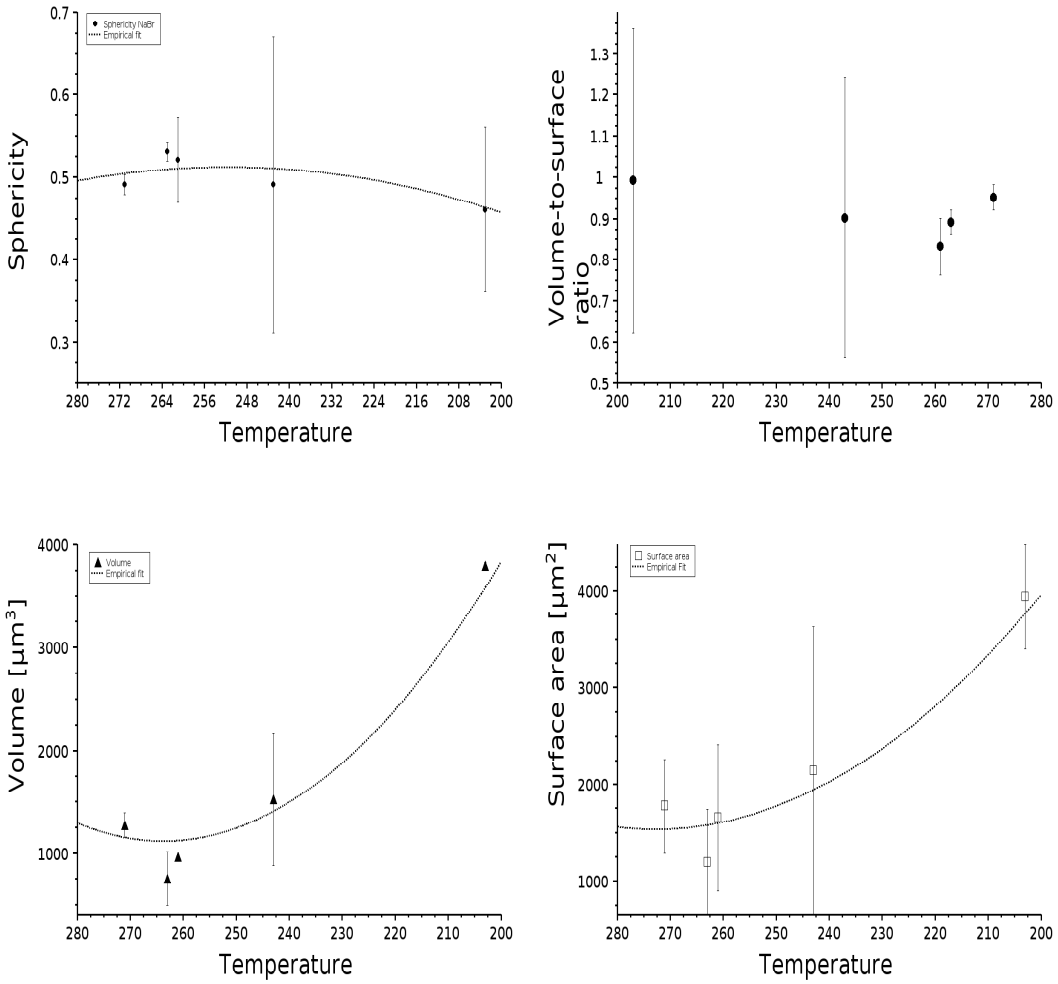


Figure 8: Geometrical characteristics of NaBr-filled inclusions with respect to temperature.

The total amount of trapped NaBr was recalculated assuming that all salt filled pores were pure, crystalline NaBr ($\rho = 3.2$ g/cm$^3$). With decreasing exposure temperature the detected amount of NaBr increased from 1.93 $\times 10^{-6}$ g to 5.5 $\times 10^{-6}$ g.

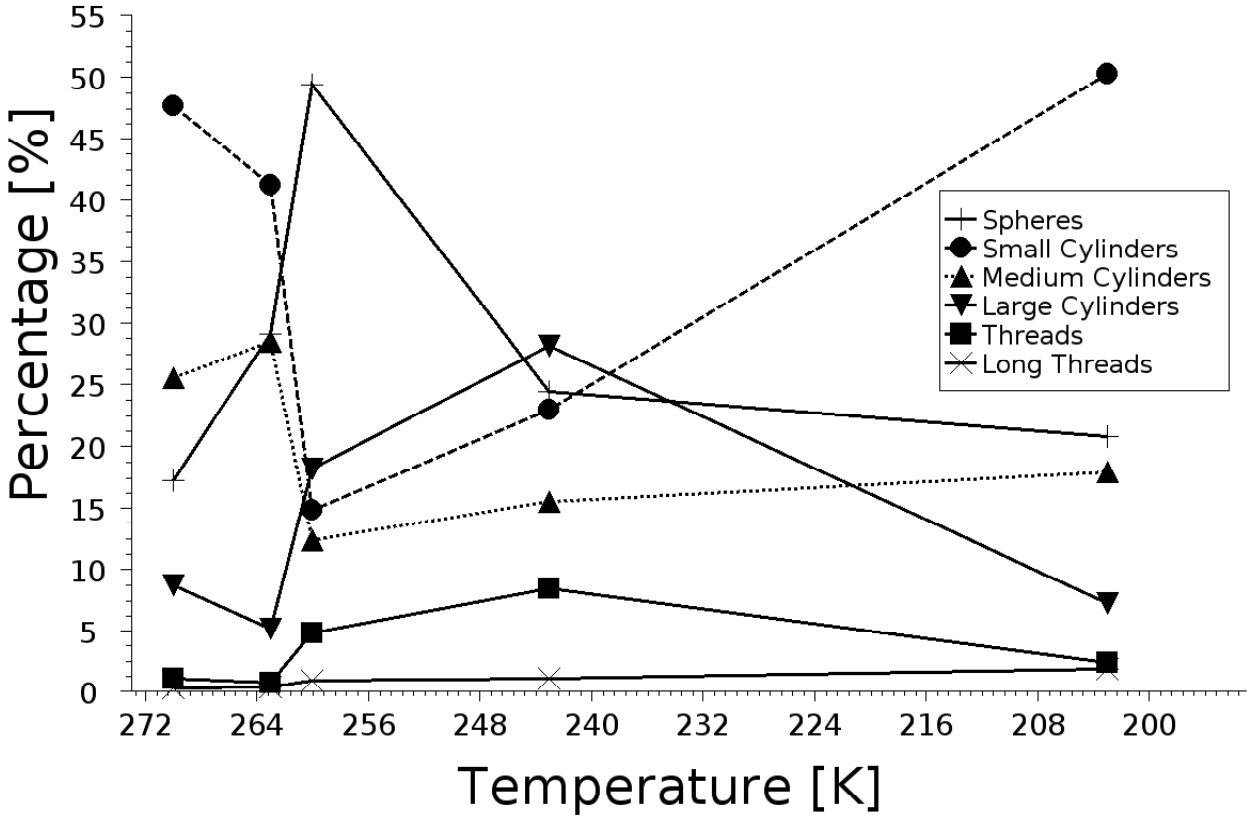


Figure 9: Changes in the morphology of the trapped NaBr-filled inclusions with respect to temperature.
For this analysis the sphericity of each pore was determined and sorted into bins. The bin sizes were determined by assuming ellipsoidal objects with different ratios of the major axes and calculating their sphericity (cf. legend above).

**CSD-analysis of the NaBr-filled inclusions** The population-density of NaBr-filled inclusions is presented in Figure 10. This plot shows a small (less than 5% of all pores) non-linear part which may have formed due to occasional accumulation of NaBr precipitates. This slightly convex downward shape seems to be common for most natural samples. However, the non-linear part has been neglected due to its small percentage of the total number of pores.

Table 3: Geometric characteristics of the NaBr-filled inclusions with respect to temperature.
$G^{approx}$ and $J^{approx}$ are the approximated growth and nucleation rates in terms of volume ($mm^3$). S is the absolute value of the first derivative of the linear fit to the population density. The amount of NaBr in grams was determined by assuming that all precipitates of NaBr were pure and perfectly crystalline with a density of 3.2 $g/cm^3$. The sphericity was determined according to the formula by Wadell (87) and describes to what extend the pore shape deviates from a sphere.

| Exposure temperature | Average volume $10^{-15}m^3$ | Average surface area $10^{-9}m^2$ | Sphericity $\Psi$ | Volume-to-surface ratio $\mu$m |
|---|---|---|---|---|
| 271 K | 1.3 | 1.3 | 0.49 | 0.95 |
| 263 K | 0.8 | 0.9 | 0.53 | 0.89 |
| 261 K | 0.9 | 1.2 | 0.52 | 0.87 |
| 243 K | 1.5 | 1.5 | 0.50 | 0.90 |
| 203 K | 3.8 | 2.8 | 0.46 | 0.99 |

| | $G^{approx}_{average}$ $mm^3sec^{-1}$ | $J^{approx}_{average}$ events $mm^{-3}sec^{-1}$ | $S_{average}$ $\mu m^{-3}$ | NaBr $10^{-6}$ g |
|---|---|---|---|---|
| 271 K | 0.2 | 0.4 | 0.003 | 1.9 |
| 263 K | 1 | 1.2 | 0.006 | 1.4 |
| 261 K | 5 | 1.2 | 0.004 | 2.4 |
| 243 K | 1540 | 160 | 0.003 | 2.0 |
| 203 K | $6.7 \times 10^8$ | $7.7 \times 10^6$ | 0.001 | 5.5 |

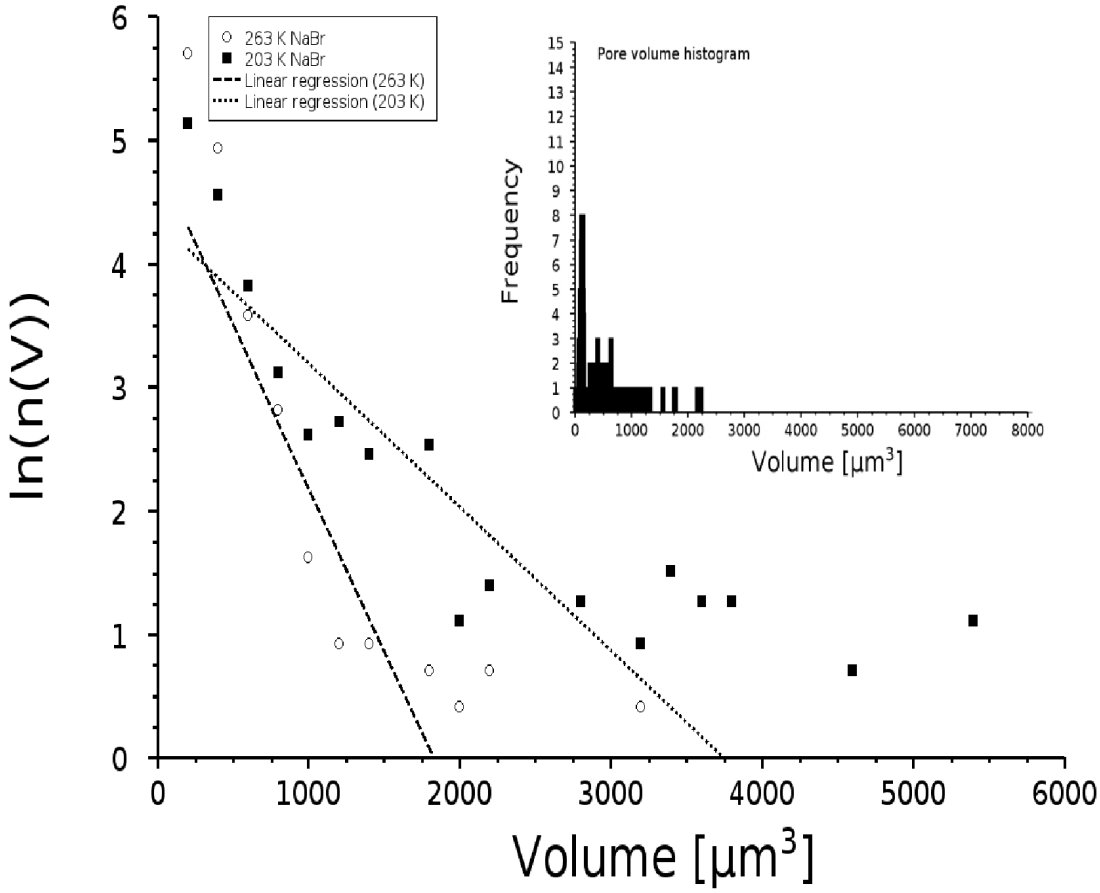


Figure 10: Normalized population density (ln(n/n°)) versus volume of the NaBr-filled inclusions.

The CSD analysis of the NaBr-filled inclusions yield the temperature dependence of the approximate growth- (G) and nucleation rate (J):

$$G_{average}^{approx} = exp^{-0.33 \times T + 87} \tag{10}$$

$$J_{average}^{approx} = exp^{-0.19 \times T + 78} \tag{11}$$

where T is the exposure temperature in Kelvin and G is reported as $mm^3$ per second. The approximate nucleation rate has the units of events per $mm^3$ and per second. The $R^2$ index was 0.90 in both fits. This clearly

indicated that the growth rate increased more slowly than the nucleation rate. The latter raised exponentially once an under-cooling of more than 30 degrees was approached which agrees well with various experimental studies as summarized by Seinfeld and Pandis (4).
In Figure 14 the initial conditions of solidification for all samples are presented. At 271 K the growth rates of the trapped inclusions were slow and nucleation events occurred rarely. But both rates increased as the exposure temperature decreased. Once a temperature of 243 K was passed, the system returned to lower rates. However, at 203 K the nucleation rate was significantly higher than at 261 K but the growth was more or less equal.

### 3.3.2 Air-filled inclusions

**Geometrical characteristics of air-filled inclusions** To some extend air bubbles behaved similarly to the just described NaBr inclusions. They occurred as rather elongated objects at 271 K and 203 K while spherical to cubical inclusions dominated at the exposure temperatures in between. Table 4 presents a summary of the geometrical characteristics of the trapped air bubbles.
At 261 K the average pore volume was $0.9 \times 10^{-15}$ m$^3$. It reached a maximum of $5.6 \times 10^{-15}$ m$^3$ at 200 K. The average surface area followed this behavior, while the sphericity reached its maximum at 261 K (Figure 11). These measurements were fitted using the following empirical equations:

$$V_{average}\ [\mu m^3] = 227863 - 1923.92 \times T + 4.06108 \times T^2 \quad (12)$$

$$S_{average}\ [\mu m^2] = 181848 - 1482.61 \times T + 3.03877 \times T^2 \quad (13)$$

$$\Psi_{average} = -4.41793 + 0.040484 \times T - 8.15888 \times 10^{-5} \times T^2 \quad (14)$$

where T is the exposure temperature in Kelvin. They reached a stability index $R^2$ higher than 0.7. At 271 K the samples had an average porosity of 0.56%, which grew to 0.80% as the exposure temperature decreased to

203 K. At 271 K most air bubbles were either spheres or small cylinders. As the exposure temperature decreased, more and more medium cylinders were formed. The number of spheres reached their minimum between 261 K and 243 K, but increased again towards 203 K. Also more and more threads formed as the exposure temperature deviated from 260 K (Figure 12). The small cylinders, however, vanished as the solution droplets were exposed to lower and lower temperatures.

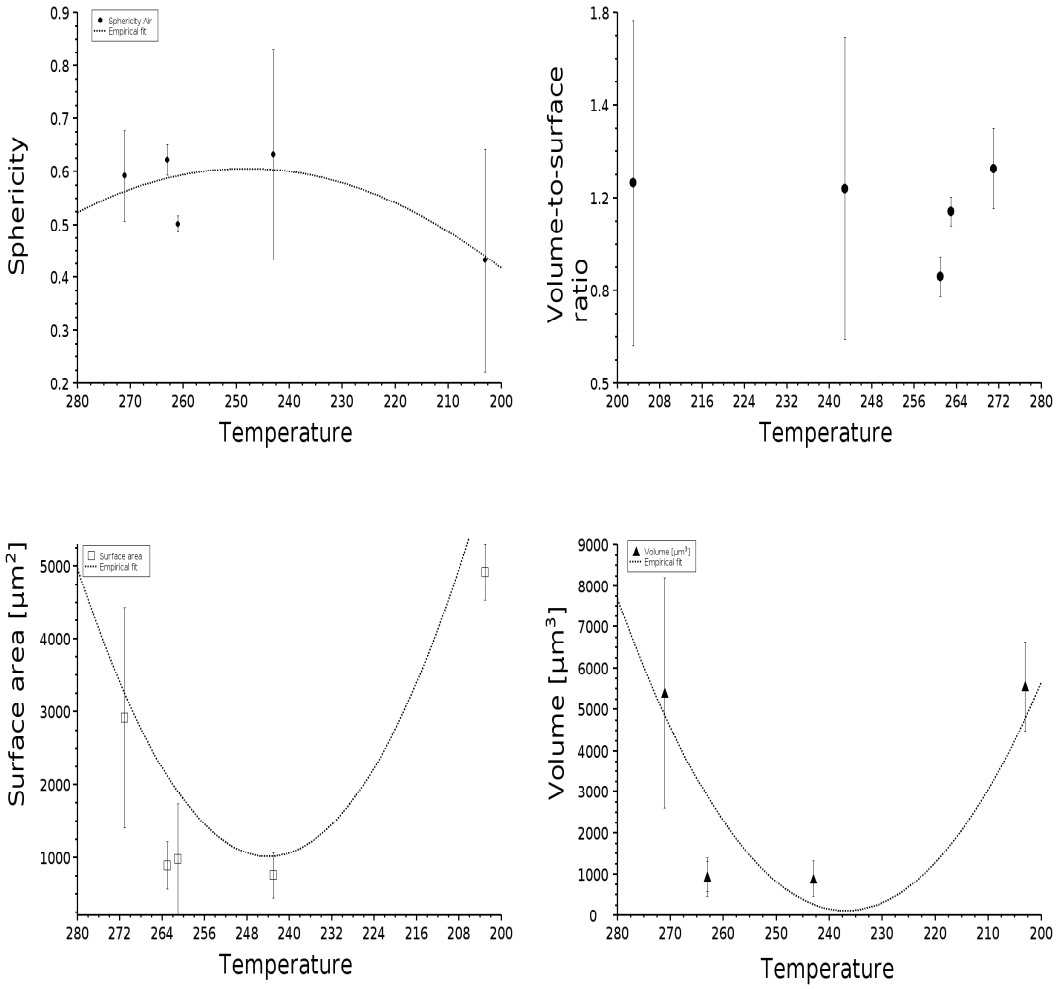


Figure 11: Geometric characteristics of air-filled inclusions with respect to temperature.

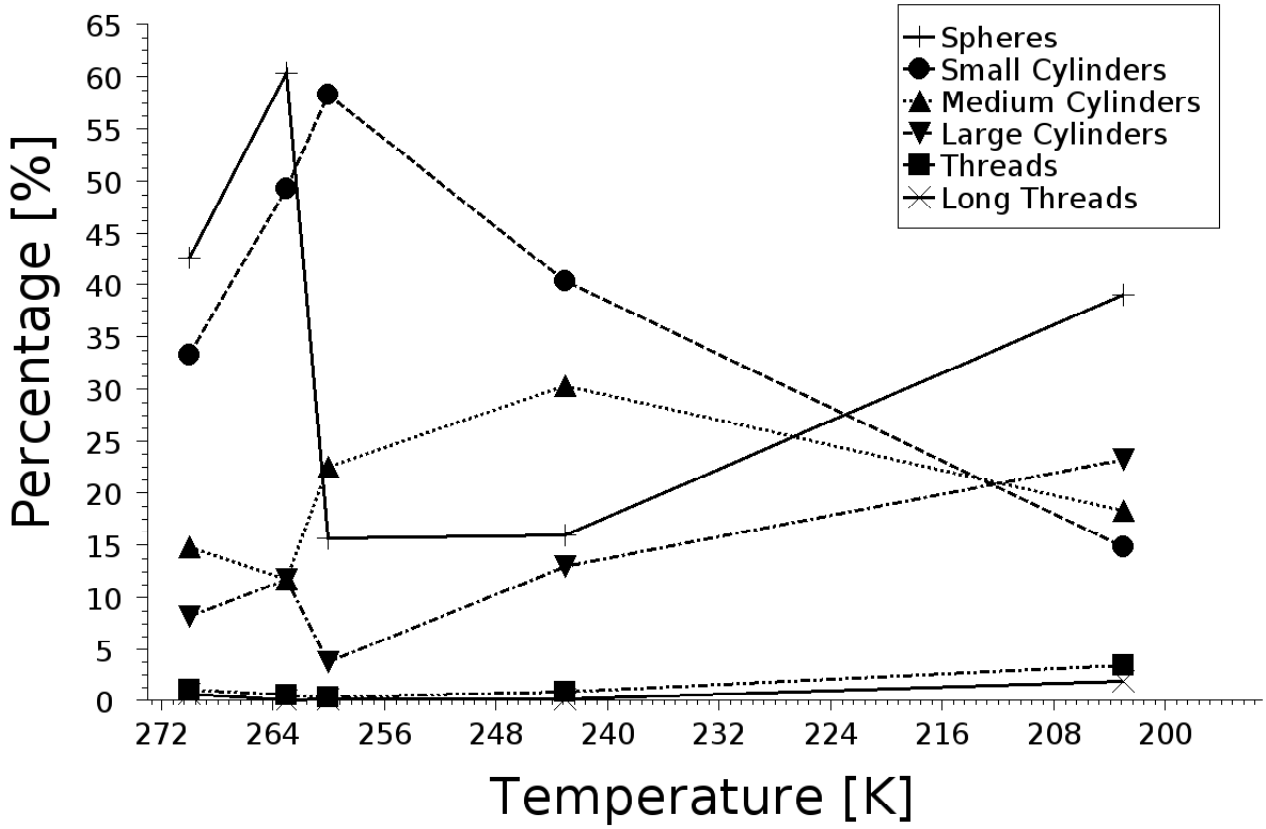


Figure 12: Changes in morphology of the trapped air-filled inclusions with respect to temperature.
For this analysis the sphericity of each pore was determined and sorted into bins. The bin size was determined by modeling the sphericity as an ellipsoidal object with different ratios of the major axes, which also yield the name of the bins (cf. legend above).

**CSD-Analysis of air-filled inclusions** In contrast to the NaBr-filled inclusions, the population-densities of the air filled inclusions moved towards lower values as the exposure temperature rose. However, in similarity to the NaBr precipitates, they showed a concave downward slope, and the non-linear tailing in Figure 13 was caused by less than 5% of all pores which allowed deriving S (absolute value of the population-density slope) from a linear fit.

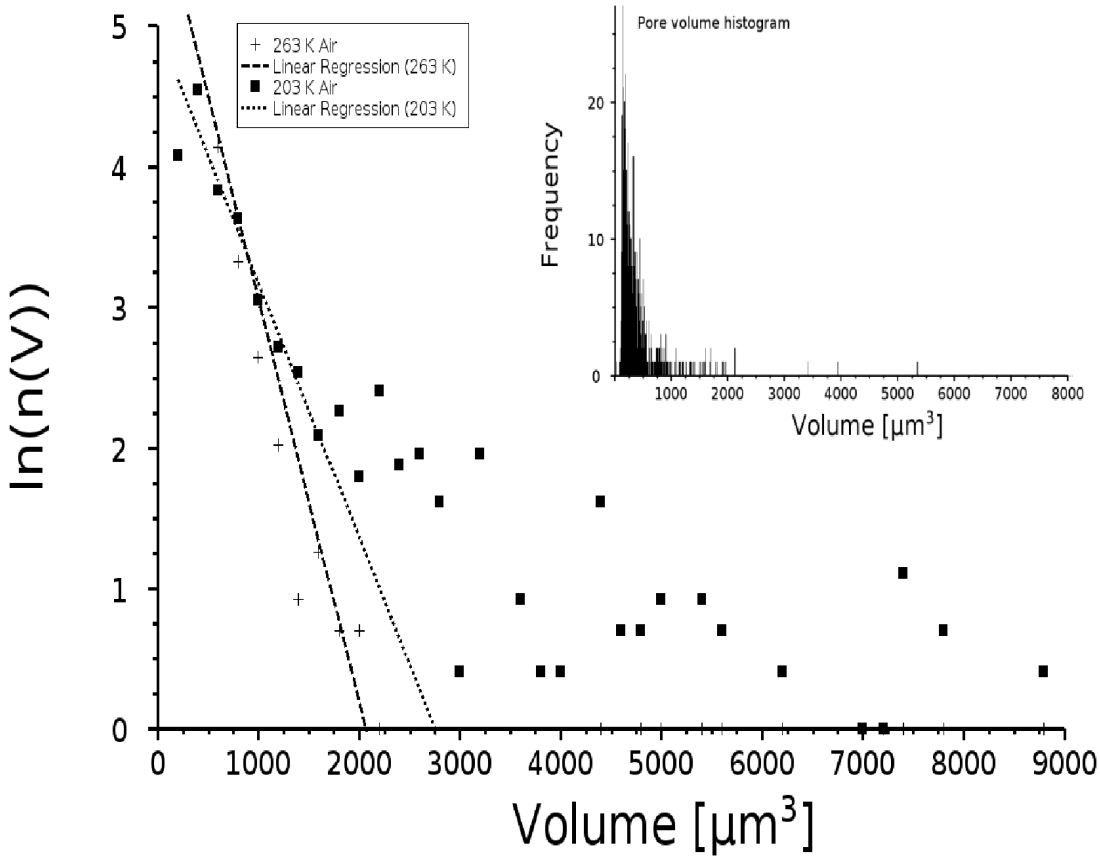


Figure 13: Normalized population density (ln(n/n°)) versus the volume of air-filled inclusions.
As the exposure temperature decreases the population-densities tend to higher values.

The CSD analysis of the air-filled inclusions yield the temperature dependence of the approximate growth and nucleation rate. $G^{approx}$ and $J^{approx}$

were calculated in the same manner as discussed for the NaBr precipitates. The following temperature dependences were found:

$$G_{average}^{approx} = exp^{-0.32 \times T + 84} \tag{15}$$

$$J_{average}^{approx} = exp^{-0.29 \times T + 76} \tag{16}$$

where T is the exposure temperature in Kelvin and G is reported as $\mu m^3$ $sec^{-1}$. The approximate nucleation rate (J) is reported as events $\mu m^{-3}$ $sec^{-1}$. The $R^2$ index was 0.98 in both fits.

The initial conditions of solidification are summarized in Figure 14. In contrast to the NaBr-filled inclusions a hysteresis-like curve resulted from the CSD-analysis of the air bubbles. Also the difference between the lowest and highest degree of under-cooling is less severe compared to the salt inclusions. The highest nucleation as well as growth rates were found at 261 K.

Table 4: Geometrical characteristics of the air-filled inclusions with respect to temperature.
$G^{approx}$ and $J^{approx}$ are the approximated growth and nucleation rates in terms of volume ($mm^3$). S is the absolute value of the first derivative of the linear fit to the population density. The porosity was calculated as volume occupied by gas over total volume of ice. The sphericity has been determined using the formula by Wadell (87) describing the deviation of the actual pore shape from a sphere.

| Exposure temperature | Average volume $10^{-15}$ $m^3$ | Average surface area $10^{-9}$ $m^2$ | Sphericity $\Psi$ | Volume-to-surface ratio $\mu$m |
|---|---|---|---|---|
| | | Air | | |
| 271 K | 5.4 | 2.1 | 0.59 | 1.3 |
| 263 K | 0.9 | 1.4 | 0.62 | 0.6 |
| 261 K | 0.9 | 0.9 | 0.88 | 0.5 |
| 243 K | 0.8 | 1.1 | 0.63 | 0.8 |
| 203 K | 5.5 | 6.9 | 0.43 | 0.9 |

| | $G^{approx}_{average}$ $mm^3sec^{-1}$ | $J^{approx}_{average}$ events $mm^{-3}sec^{-1}$ | Porosity % | Inner-to-outer surface |
|---|---|---|---|---|
| 271 K | 0.5 | 0.1 | 0.56 | 0.14 |
| 263 K | 1 | 3.8 | 0.49 | 0.07 |
| 261 K | 3 | 17.7 | 0.43 | 0.25 |
| 243 K | 880 | $6.9 \times 10^3$ | 0.33 | 0.19 |
| 203 K | $6.4 \times 10^8$ | $5.5 \times 10^7$ | 0.08 | 0.25 |

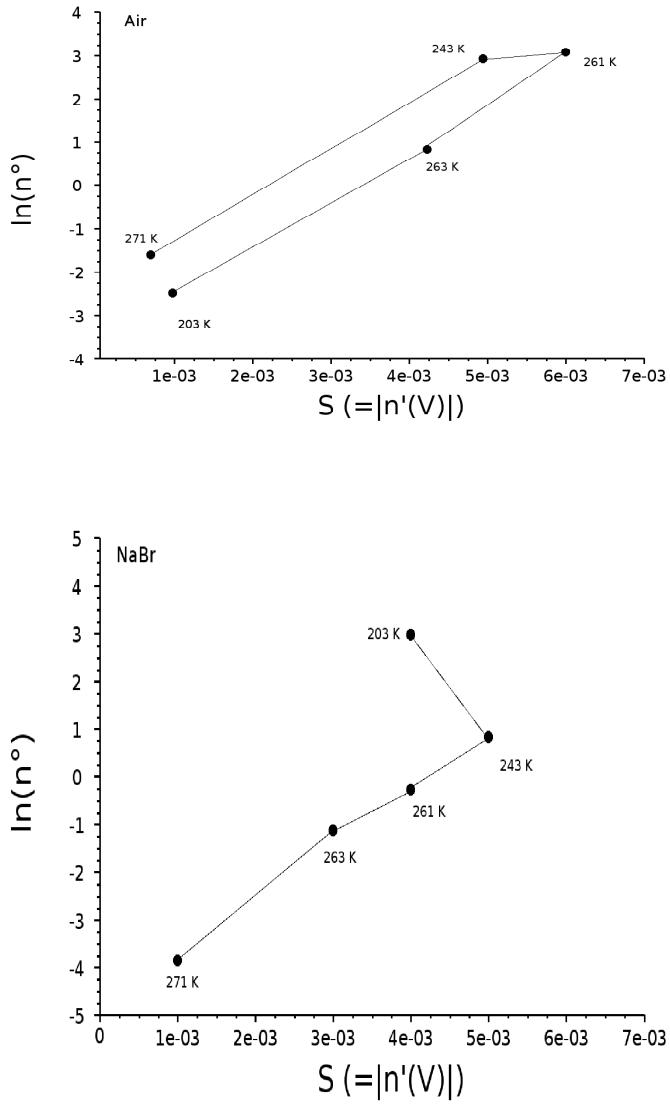


Figure 14: Comparison of initial growth- and nucleation rates.
The growth and nucleation rates for air bubbles are presented on the top, while those of the NaBr precipitates are shown at the bottom of this figure.

## 3.4 Multiphase and mixed systems

### 3.4.1 Octanol/$H_2O$ emulsion

Octanol, a common proxy for liquid organic urban aerosols (5; 102; 103; 104; 105), could be clearly identified by the contrast change at the ice-octanol phase boundaries (Figure 15). Yet, the very low contrast between air and octanol inclusions did not allow distinguishing between these two substances. The organic solvent occupied a total volume of 4.1 $\times 10^{-7}$ $m^3$. The average surface area was found to be 2.5 $\times 10^{-12}$ $m^2$. The average sphericity reached a value of 0.59, while the volume-to-surface ratio was 2.7 $\mu$m.


Figure 15: Octanol inclusions in ice frozen from an emulsion of MilliQ-water and octanol. This formulation was prepared by shaking a mixture of octanol and water in a clossed vessel with some head space for 24 h. For clarity only a small section of the total sample is presented.

### 3.4.2 Octanol/$H_2O$/NaBr emulsion

If 1 wt.% of NaBr was mixed with octanol prior to freezing, the shape of the resulting inclusions in the frozen sample changed significantly. The convex walls of the ice-octanol boundaries as observed for the pure solute, turned into concave ones (Figure 16). The total surface area and total volume also increased compared to solute samples without NaBr. The octanol/brine inclusions formed a very narrow and curly network throughout the whole sample, occupying an average surface area of 8.1 $\times 10^{-9}$ $m^2$ and an average volume of 2.2 $\times 10^{-14}$ $m^3$. The average sphericity increased to 0.63 compared to the pure octanol/$H_2O$ system, while the volume-to-surface ratio decreased to an average value of 1.6 $\mu$m.

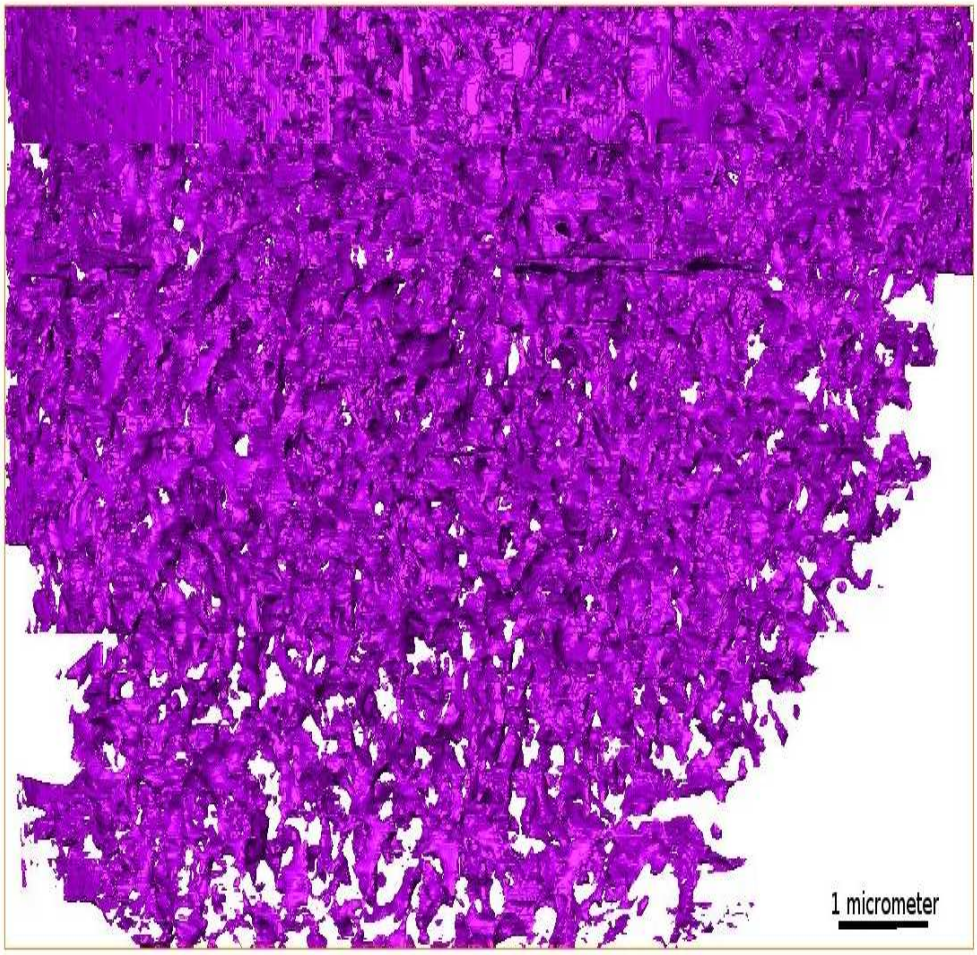


Figure 16: Octanol-brine inclusions in ice frozen from an emulsion of octanol and a dilute ($10^{-4}$ molar) NaBr solution.
Like the octanol-$H_2O$ emulsion this mixture was also shaken for 24 hours in contact with air. For clarity only a small section of the total sample is presented.

### 3.4.3 Quartz suspensions

Inclusions of quartz particles were found homogeneously distributed over the whole sample (cf. Figure 17). The average volume per inclusion was 4.4 $\times 10^{-18}$ m$^3$, while the average surface area reached a value of 5.7 $\times 10^{-9}$ m$^2$. The volume-to-surface ratio was found to be 0.77 $\mu$m with a mean sphericity of 0.36.

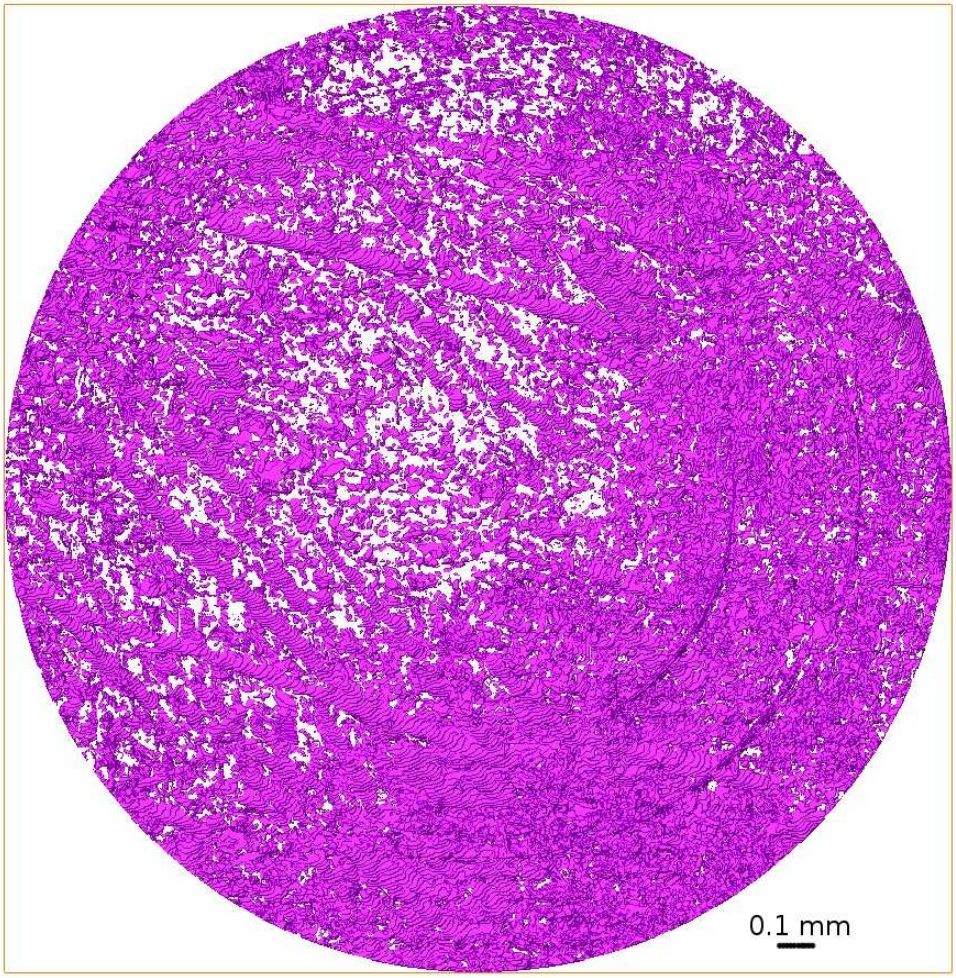


Figure 17: Quartz inclusions in ice frozen from MilliQ-water.

### 3.4.4 Quartz/NaBr suspension

Freezing quartz particles suspended in a 1 wt.% NaBr solution at a temperature of 240 K led to small, homogeneously distributed inclusions in ice (cf. Figure 18). An average volume of 6.0 $\times 10^{-16}$ m$^3$ with a surface area of 5.1 $\times 10^{-10}$ m$^2$ was found. The mean sphericity of these inclusions was 0.68, indicating a rather spherical geometry. The volume-to-surface ratio reached a low average value of 1.14 $\mu$m.

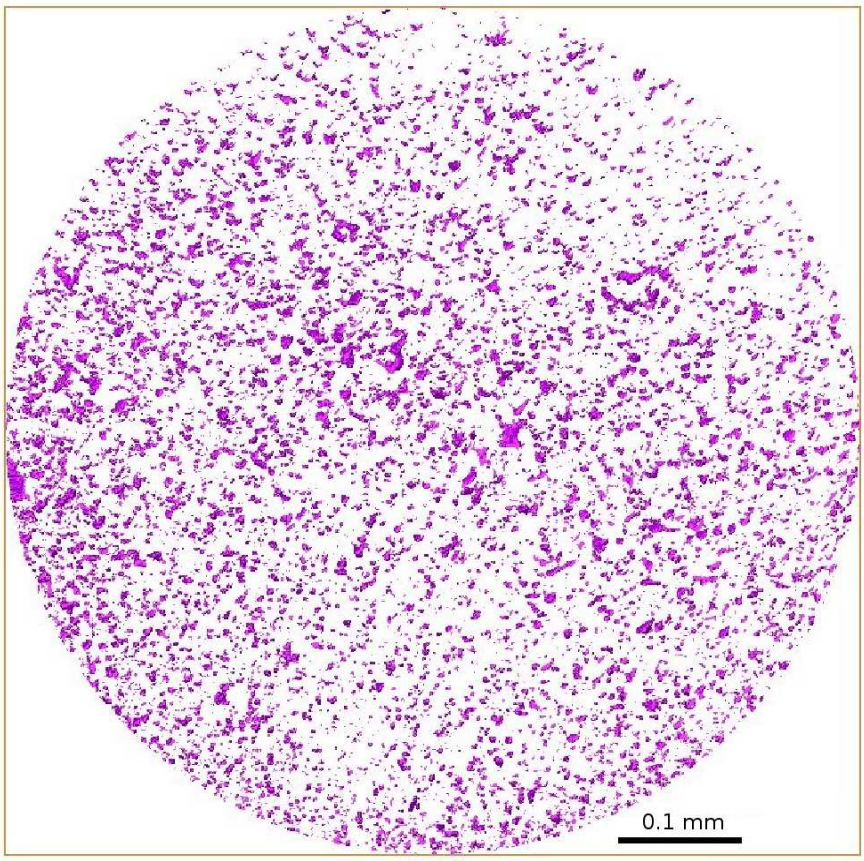


Figure 18: Quartz-brine inclusions in ice frozen from a suspension of quartz particles in a dilute ($10^{-4}$ molar) NaBr solution.

### 3.4.5 Bentonite

Figure 19 depicts the ice-trapped bentonite (clay) inclusions. The average void filled a volume of 4.4 $\times 10^{-13}$ m$^3$, with an average surface area of 1.3 $\times 10^{-13}$ m$^2$. The mean volume-to-surface ratio was 0.36 $\mu$m. The clay particles were found to be agglomerated into elongated structures of a rather low sphericity of 0.25, much less than the above described quartz inclusions.

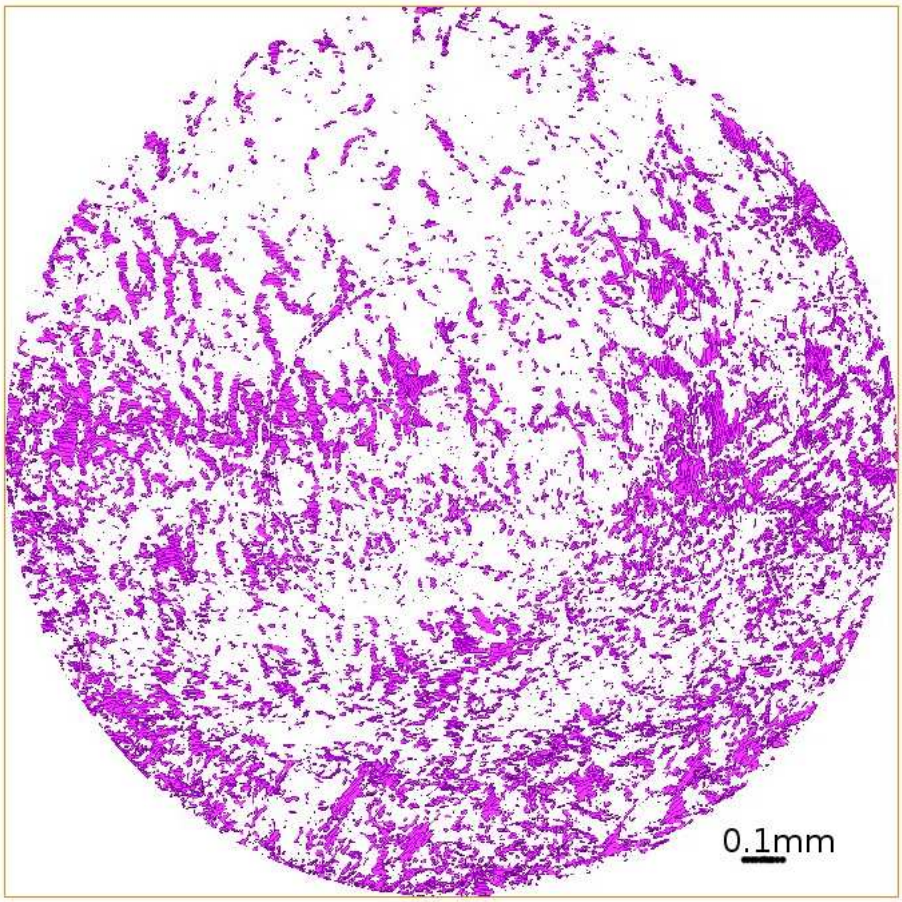


Figure 19: Bentonite inclusions in ice from a suspension of bentonite particles in MilliQ-water.

### 3.4.6 Bentonite/NaBr suspension

Bentonite inclusions showed a completely different behavior upon freezing in a NaBr solution than in MilliQ water. Long sheets, almost perpendicular to each other, were found (Figure 20). An average surface area of 6.0 $\times 10^{-9}$ m$^2$, and an average volume of 6.7 $\times 10^{-15}$ m$^3$ were determined. The sphericity reached a mean value of 0.35, with a volume-to-surface ratio of 0.79 $\mu$m.

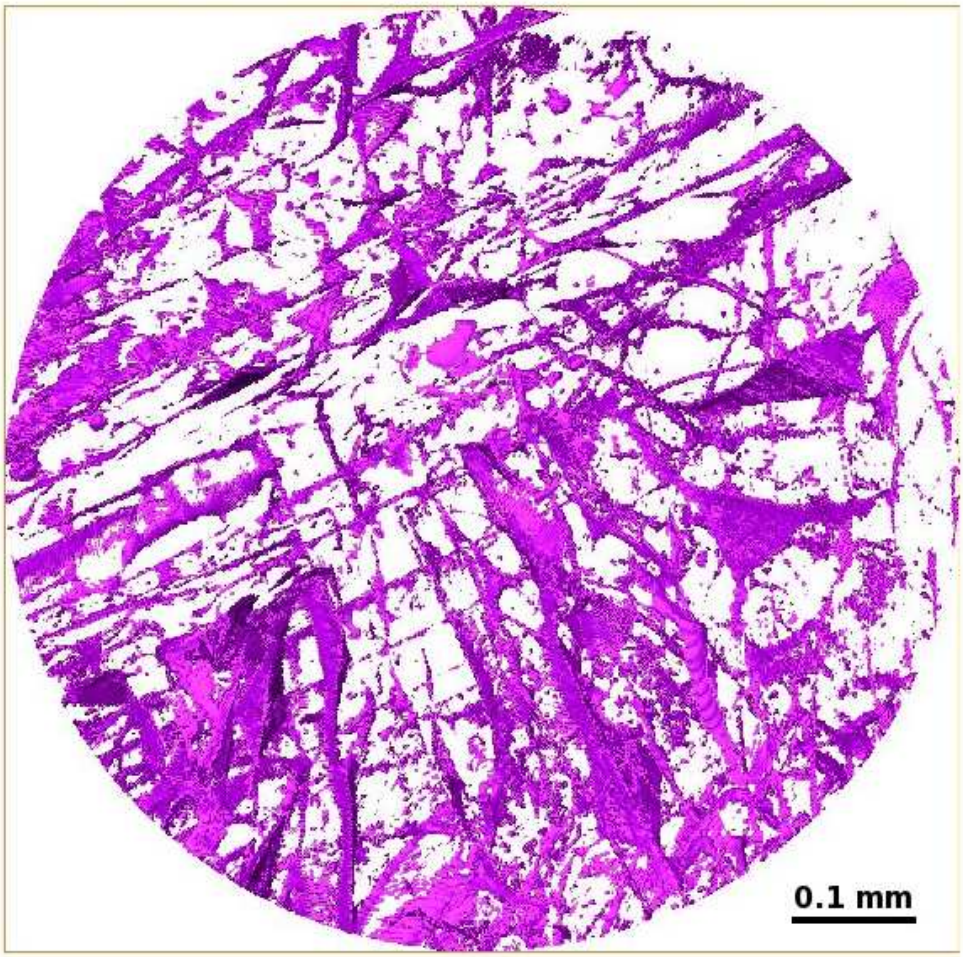


Figure 20: Bentonite-brine inclusions in ice frozen from a suspension of bentonite particles in a dilute ($10^{-4}$ molar) NaBr solution.

# 4 Discussion

## 4.1 Possible errors of the experimental setup and in the interpretation of the data

### 4.1.1 Beam and sample stability

Synchrotron-based X-ray tomography is characterized by a relatively small, parallel beam geometry. Possible beam intensity fluctuations are minimized at the SLS by means of the top-up injection mode (300 ± 1 mA) and the beam line setup (83). However, in order to correct beam instabilities, darks and flats were taken every 50 angular steps. To this end the sample holder was moved out of the X-ray beam towards the inner wall of the surrounding cage, where the temperature was slightly higher than in

the center. These were very critical moments, because temperature gradients may cause shape-metamorphism of ice (75; 98; 99). To minimize possible temperature fluctuations, the outer (warm) gas-flow was stopped 2 seconds before moving the sample. It was switched on again two seconds after the sample had been returned to the center. The intensity of the cold gas flow was kept constant at 10 L/min at all times. This procedure limited temperature changes in the sample holder to less than 3 degrees as recorded by the PT-100 element. But, the temperature sensor was mounted at the bottom of the sample holder and had a much better thermal contact to the surrounding gas than the ice sample. Moreover, this sensor was embedded in a glue of lower isolating capacity compared to the sample holder itself. The high heat capacity of the organic matrix, and the relatively thick polyamide walls additionally helped to stabilize the sample thermally.

These isolation effects were corroborated by heating rate estimates of the upper limits for temperature changes of the sample holder. Therefore, a fully prepared polyamide cup was frozen at 240 K and then suddenly exposed to room temperature. As 263 K were never reached within less than 40 seconds during those runs, the heating rate was determined to be below 0.6 K/s. Thus, the maximum temperature change, as recorded by the PT-100 element at the bottom of the sample holder, could not exceed 3.6 degrees during the 6 seconds required for a full darks and flats imaging run. The measured temperature fluctuation poses an upper limit to temperature variations during the experiment.

Also, the cold gas flow, which left the Kapton cage, was directed towards the micro-mechanics of the goniometer stage. An additional isolating stainless steel tray was mounted at the bottom of the sample support (Figure 1) to avoid water condensation from the ambient humidity on this sensitive equipment. Depending on the humidity inside the experimental hutch a pump was added to suck the cold gas stream away from the goniometer stage and so further reduce the possibility of condensation. Such con-

densation would have disturbed the smooth and precise movement of the sample-holder during the scan and therefore it would have reduced the quality of the resulting projections.

### 4.1.2 Sample metamorphism

The two major possibilities when shape metamorphism (70; 72; 73; 74; 75; 76; 77) may have occurred to the presented samples were during the time, when the samples were stored in dry ice or during the transport in the well isolated electrically cooled box (240 K) from the Jungfraujoch to Mainz. Cabanes et al. (77) as well as Colbeck (75) showed that the rate of isothermal recrystallization of ice particles strongly decreases with decreasing temperature. Therefore, it cannot neglected that the samples might have changed to some extend. However, the results of this study suggest that the metamorphism had no detectable effect at the spatial resolution obtained. If recrystallization had taken place, the air-filled voids inside the samples should be different compared to the obtained pictures, because the progressing metamorphism would lead to Ostwald ripening (a broadening of the ice crystals) and a complete expulsion of air from the sample (75). This process can easily be seen in strongly recrystallized snow (private communication with M. Schneebeli) and was confirmed as hail stone 1 was forced to metamorphose while heating it to 265 K. Additionally, Y-shaped pores were found in the particles from the Jungfraujoch, indicating negligible changes during transport.

All the other experiments focussed on the morphology of inclusions and not on the shape of the ice particles. This assigns possible metamorphism of the particle-surfaces only a minor role with respect to the interpretation of the obtained data. Besides, the metamorphism experiment of the salt-solution sample yielded detectable changes in pore-volume and morphology, which should not be possible in highly metamorphosed samples.

### 4.1.3 Sensitivity of the experimental approach

The fraction of not-detected pores in the samples was estimated as follows. The total volume occupied by any type of inclusion was determined at spatial resolutions ranging from 14 $\mu$m to 1.4 $\mu$m. Therefore the experimental data were software-binned using the provided routines and a Lanczos-Filter (85) of AMIRA. In Figure 21 a plot of the change in segmented volume with respect to the voxel size is presented. At a spatial resolution of less than 5.2 $\mu$m the slope is more or less flat in this logarithmic plot, indicating that from this point onwards the increase in segmented volume is extremely small. Assuming that this increase in volume will stay constant as the spatial resolution decreases further, the theoretically possible void-volume detectable with 10 nm large voxels was calculated. Comparing this with the values obtained for 1.4 $\mu$m showed that 95% of the total pore volume can currently be detected.

### 4.1.4 Mass balance calculations

The results of the performed mass balance calculations deviate from the expected concentrations for several reasons:

1. Uptake of air or NaBr into the ice crystals
2. Trapped volumes, which are significantly smaller than the spatial resolution
3. Only pores with a diameter larger than 3 voxels were considered

The first argument only explains a very tiny fraction of the missing impurities, because the partitioning coefficient of air and NaBr between ice and water is on the order of $10^{-3}$ (solid to liquid). The possible uptake of these substances into the ice lattice is discussed elsewhere in detail (9; 10; 92). The second point is of higher importance. The CT-numbers of ice vary over a wide range. This is mainly due to the trapping of inclusions which are significantly smaller than the voxels and therefore result in mixed-pixel

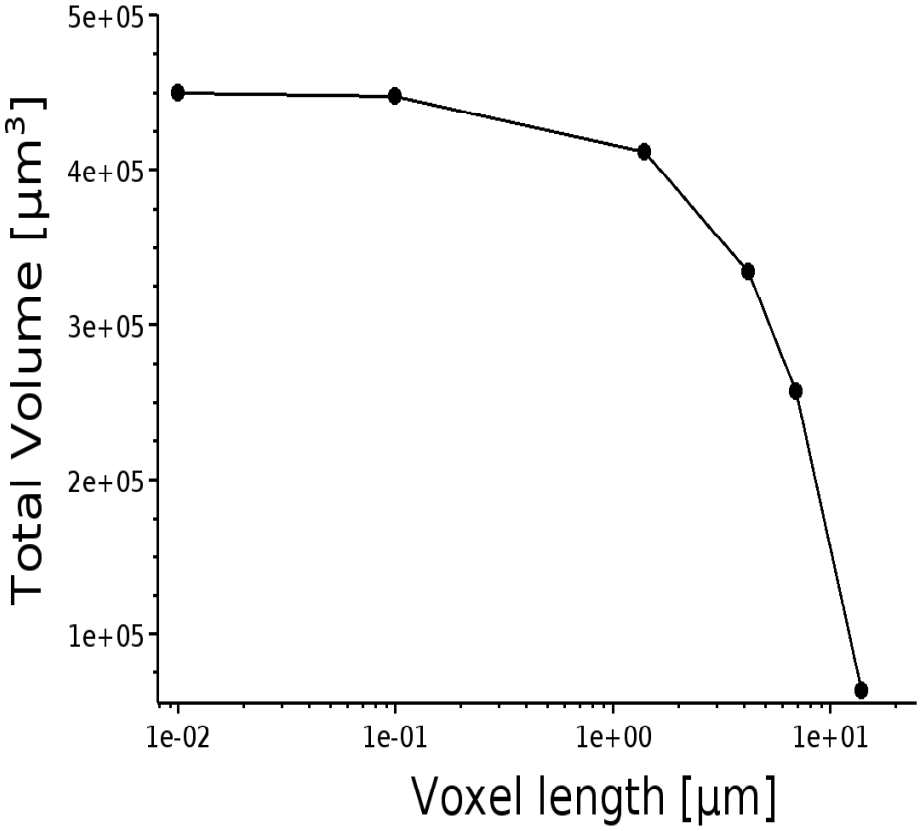


Figure 21: The total volume of NaBr-filled inclusions versus various spatial resolutions. Note the plateau-like level, once the voxel length is below 5.2 $\mu$m. As an example, data of the NaBr solution sample before its metamorphism are presented (Section 2.1.2 and 3.2).

information. The same argumentation is true for the inclusions of NaBr. A high number of precipitates smaller than the spatial resolution explains the heterogeneity of the ice matrix.

Finally, only segmented elements with a diameter of more than three voxels were accepted as voids in order to further improve the signal-to-noise ratio. These three arguments satisfactorily explain the missing fractions of air or NaBr in all the samples presented.

## 4.2 Natural samples and the metamorphism experiments

### 4.2.1 Natural samples

No impurities apart from air could be detected inside the grains. Ionic compounds, if present, are expected to be at such a low concentration that no significant absorption contrast could be gained. Solid particles, like mineral dust, known to act as ice nuclei, were completely absent, or well below the voxel resolution of 1.4 $\mu$m in these two samples. Distinct zones of higher air bubble density (ABD) and lower ABD were reported in the literature for hail stones of several mm to cm in size (45; 106; 107; 108; 109), but were not found in the presented samples. In addition, the size of the single ice crystals could not be determined, which makes a direct comparison to these studies difficult. The density of the hail stones fits well into a compilation of data given by Pruppacher and Klett (17). Additionally, the outer morphologies of the samples agree well with those reported 40 to 50 years ago (45; 106; 107; 108; 109). But those samples had grown to diameters of several centimeters.

Hail stone 1 (collected at Mainz) shows a unique distribution of the air-filled inclusions before metamorphism. All voids were trapped in onion-like layers (92). Their Y-shaped morphology was also seen in the Jungfraujoch samples. However, in the latter, the voids neither occurred in a preferred orientation nor in only one part of the sample. On the other hand, the preservation of these features indicates that shape metamorphism, as it might have occurred to our samples, could not be detected at the current spatial resolution.

All natural ice particles showed homogeneous distributions of air bubbles throughout the samples. Especially in the case of the Jungfraujoch particles two major classes of pores could be identified optically: a) rather small inclusions and b) large bubbles. Since both types of inclusions were distributed all over the samples, one can hardly speculate about different origins of these voids.

A higher spatial resolution is required to elucidate whether the air bubbles identified are connected to the outer surface of the samples. Liquid water (17) which is known as a possible constituent of such samples, could not be detected.

**Morphology of air- and salt-filled inclusions** Spherical gaseous inclusions are well known from past studies using 2D-optical-microscopy. Typically, gas bubbles ranging from about 20 - 500 micrometers in diameter were observed (92; 110). In the NaBr solution sample not only spherical voids, but also sheet-like structures were found. Similarly to the air bubbles, the NaBr inclusions were trapped in various morphologies. The ice crystals, however, could not be determined allowing the reconstruction and identification of the vein network. The V-shaped inclusions resemble triple junctions, which were found in ice at temperatures close to the melting point (51).
While the formation of spherical and round inclusions was discussed theoretically and on experimental basis (92; 110), little is known about the formation of the elongated, cylindrical voids. Their origin is probably related to the velocity of the dendritic growth of ice crystals. The build-up of a "mushy layer" at low growth rates and high salt concentrations (111; 112; 113), may also be responsible for these structures.

### 4.2.2 Metamorphism experiments

In the metamorphism experiment of the NaBr-doped sample a phase transition from solid to liquid and back to solid was triggered by raising the experimental temperature above the eutectic point of the NaBr-$H_2O$ system. This transformation started at the NaBr-ice interface. As soon as the first melt formed, it expanded along the grain boundaries and lead to the formation of veins (51; 114; 115). This process was reversed by lowering the experimental temperature to 230 K again. The salt solution was expelled from the growing ice and further concentrated. Locally, this lead to very high super-saturations and to the precipitation of salt crystals. With this

process, one can easily explain an increase in the total number of salt-filled voids.

In the case of air bubbles the situation was more complex. Their total number increased, but their total volume decreased. During the metamorphism, their average pore volume and average surface area shrank even more drastically, while their sphericity grew.

In principle two processes may account for the change in total volume occupied by air. First, some air got dissolved in the freshly formed melt and transported towards the surface of the sample (step 2 in Figure 5). While the experimental temperature returned to 230 K, a certain amount of the gas-phase could even have been expelled from the sample. This however, seems to be less likely, because it would require the formation of a liquid film to provide a high enough transport capacity for air from the bulk of the sample to its surface.

A more favorable scenario is that the partly dissolved gas in the NaBr-$H_2O$ melt nucleated in tinier bubbles during subsequent cooling. This is corroborated by a slight decrease in average pore volume in the metamorphism experiment with hail stone 1. The decrease of air-filled void volume in the natural samples is small because it is strongly related to the concentration of impurities in the ice. These should be present at such extremely low concentrations that they could not be detected. So, significantly less melt formation occurred during the heating. As less melt forms, less air can dissolve in the liquid phase. Therefore, the volumes of the trapped air bubbles inside the hail stone did not vary as strongly as in the salt solution. Irrespective of which scenario may be favored, the measured changes show that initially larger air bubbles decompose into smaller ones. To fully elucidate this process a higher spatial and a higher time resolution would be necessary.

The lack of two or even three-phase inclusions, like air and salt or air, salt and solution together in one void is surprising. On the one hand, the mechanisms of trapping NaBr and air are different. Differences in the energy

required to form a critical germ for nucleation, buoyancy, settling rate and interface-energies or even heterogeneous nucleation on ice surfaces may be responsible (116). On the other hand, the growth rate (recrystallization rate) of the liquid phase determines if pores are pushed ahead of the solidification front or buried. The faster the ice grows the larger the particle or bubble can get that stays ahead of the crystal (117).
It is interesting to note that the sphericity of all inclusions, regardless of their chemistry, is very high after the metamorphism, indicating the formation of rather spheres and small cylinders from initially more complex morphologies. A certain degree of coarsening of the NaBr inclusions can be seen from the reconstructions (Figures 5 and 6).

### 4.3 Temperature dependence of inclusion trapping

Crystal Size Distribution analysis (CSD) is a well established tool for textural analysis (58; 68; 91; 118). It allows, to obtain great insights into the solidification history of the investigated sample. By plotting the initial nucleation versus the growth rate (Figure 14) the initial conditions of the solidification process of the sample can be deduced. At the highest experimental temperature (271 K) both rates were very low, because the ice grew slowly (only a few mm/sec. (80)). As the under-cooling increased, the ice crystals grew faster and higher supersaturations were achieved locally. Furthermore, a lower exposure temperature increased the nucleation rate. This forced the nucleation and growth rate of the finally trapped voids to increase. A maximum of this process was reached at temperatures between 260 K and 240 K. As the exposure temperature decreased even further the salt content of a brine, in contact with an ice crystal, became higher. This increase in salinity led to a severe melting point depression and therefore slowed the growth rate of the ice crystals (80; 81; 116; 119) which finally led to the enclosure of thread-like voids filled by either highly concentrated brines or air. At the same time as an inclusions started to get trapped, a little bit of accumulation occurred as well (110).

Pruppacher (80; 81) measured growth rates of several cm/s for temperatures at and below 243 K. This clearly excludes the formation of a "mushy layer", which could be an other possibility to trap large volumes during the solidification of various substances, including ice (100; 112; 113; 120; 121; 122; 123; 124; 125; 126; 127; 128; 129; 130; 131). The experimental results of Pruppacher (80) examining the growth of ice from a $10^{-4}$ molar NaBr solution show rates of several cm/s at temperatures slightly lower than 243 K The growth rates of this early study are in good agreement at temperatures with the growth rates estimated for the inclusions from our experimental data. At high exposure temperatures low rates from 1 to 6 $mm^3s^{-1}$ while at the lowest exposure temperature (203 K) up to 70 $cm^3/s$ were found. Only at approximately 260 K significantly lower growth velocities are predicted by the CSD theory. This is not surprising, because one has to take into account various effects that slow down the growth rate of the ice locally. These will now be discussed.

Given that ice grows from the surface of the droplet inwards (4; 17; 32; 132) convection could have been forced as well as induced by the temperature gradient (cold surface, warm interior of the droplet. However, if significant convection would have occurred during freezing, the size of the trapped inclusions within each sample should be equal at all exposure temperatures. It would not have been possible to build up a super-saturation profile large enough to account for the trapping of impurities nor even to explain the variation in size shown here.

Besides convection heterogeneous nucleation of the salt precipitates as well as the air bubbles on the growing ice surfaces has not been considered, yet. It certainly occurred, but its influence cannot be estimated at present. But, it may explain the observed morphological changes and will be investigated with further experiments at the newly available high-speed tomography beam line (TOMCAT) of the Swiss Light Source in the near future.

Finally, latent heat effects, as they are known for crystal growth (17; 119; 133; 134) as well as pore-dragging (130; 135; 136; 137) were neglected

for the interpretation of the experimental results. Especially at 271 K latent heat effects influenced the growth rates of the individual dendritic ice crystals. The thermal conductivity of solid water (ice) is significantly higher than that of liquid water (138). This implies that the latent heat of crystallization will finally slow down the growth rate of ice since it cannot be conducted away fast enough at low degrees of under-cooling. On the other hand, the critical radius of a particle/bubble dragged along with the crystallization front depends on the speed at which this front progresses (130; 135; 136; 137; 139). Combining the last two effects would result in the formation of a cylindrical bubble partly overgrown and still propagating along with the solidification front until finally the amount of air or salt diffusing towards the inclusions is too small to allow further growth as seen in the samples frozen at an exposure temperature of 271 K.

Nevertheless, it is surprising that no two-phase inclusions (salt and air) have been found. This suggests that the nucleation mechanisms for air bubbles and salt precipitates are different. Besides, energetic differences may also account for the missing two-phase inclusions.

Like in many studies on the growth of ice from the vapor phase (4; 17; 140, and reference therein) the obtained experimental values exhibit a severe change at approximately 260 K. It is commonly reported (141, and references therein) that the shape of the crystals changes from plates to columns to plates as the surrounding temperature decreased. However, since all these studies focussed on growth from the gas phase a direct connection to growth from the liquid phase is hard to make (116). Pruppacher (80; 81) did not mention any observation of changes in crystal shape his growth rate experiments. Once, the dendritic growth rate was higher than the temporal resolution of this experimental setup, he reported the growth mode as "bulk growth". This, however provides no reliable basis to venture a comparison with studies in which the ice grew slowly from the gas phase. A possible change in the crystal shape in the samples analyzed in this study can not be ruled out. However, doubts exist that a change from plates to

columns to plates caused the large inclusions at 271 K and 203 K, because of completely different electrostatic conditions at the solid-liquid interface during growth (116; 142).

## 4.4 Multi-phase and mixed systems

Quartz, bentonite, and octanol, as well as mixtures of these components with a 1 wt.% NaBr solution were frozen at an exposure temperature of 240 K. The specific surface areas, shapes, and other geometric parameters were significantly different among the various samples studied. These differences depend on the chemistry of the impurities, as adding a salt to the solution or changing the mineral type had profound effects.

In the case of freezing pure octanol/water emulsions, spherical inclusions of the octanol were found, which are caused by the strong hydrophobicity of octanol. However, once an emulsion of a NaBr solution with octanol was made, the surface tension of the salt solution was higher compared to that of pure water (143; 144) which obviously influenced the shape and distribution of the octanol inclusions. The latter formed a highly concave and well-connected network if NaBr was present, but were convex if the salt was absent. Furthermore, air bubbles could not be identified, which suggests that all the air could be dissolved in octanol. In addition, all NaBr-precipitates were found mixed into the octanol inclusions. The connectivity of this void network allows for transport and further chemical reactions inside ice particles, and therefore may alter the chemical behavior of such particles with respect to the surrounding gas phase as well as during contact with other solution droplets or changes in temperature.

Bentonite and quartz particles formed inclusions homogeneously distributed all over the sample, but of different shape. Both minerals showed a tendency towards agglomeration when they were mixed into a diluted salt-solution. This is probably related to the difference in surface tension, which occurred due to the addition of the salt. In particular, in the case of bentonite, one may speculate that also colloidal charging effects forced the

inclusions to a more or less perpendicular orientation to each other inside the ice grain matrix. The formation of pockets filled by highly concentrated brines occurred during freezing at low growth rates and also significantly influenced the morphology and distribution of the trapped inclusions (113).

# 5 Conclusions and outlook

Synchrotron-Cryo-XMT was performed on various types of samples. For these experiments, a new setup was developed. It consists of a polyamide-cup, a cryojet, and a double-walled Kapton-foil cage. By embedding the sample in cycloheptane inside the polyamide-cup, the ice particles are not only fixed mechanically, but also favorably isolated against temperature fluctuations. Experiments can be performed at temperatures as low as 230 K with an accuracy of $\pm$ 1 K and a stability of 3 K. To avoid icing in the path of the beam, all important parts are permanently flushed with dry gaseous nitrogen. A spatial resolution of 1.4 $\mu$m was achieved in 90 minutes per scan.

Natural as well as artificial samples were analyzed with this setup. Scanning hail stones collected at the university campus on Mainz and ice particles from the Jungfraujoch proved that the current setup is well suited to detect air-filled inclusions inside natural samples. But, no other impurities have been found which may be due to two reasons. Either ionic impurities, like acids (e.g.: HCl or $H_2SO_4$) were of such low concentration that they did not cause a detectable X-ray adsorption, or these inclusions were well below the spatial resolution and disappeared within the experimental noise. Pseudo 4D-experiments were performed by heating one of these samples. So the changes in void-morphology with respect to metamorphism were elucidated. To monitor how salt inclusions move under such conditions the experiment was repeated with a NaBr solution droplet. Here, a significant transport along grain boundaries could be traced. These two experiments clearly extend the initial goal to elucidate the dependence of

void-morphology with respect to temperature and chemical composition. Such data sets form the basis for further experiments showing how the physico-chemical properties of a doped ice particle change due to metamorphism.

Apart from hail stones also droplets of a diluted NaBr solution, which were exposed to temperatures ranging from 271 - 203 K for freezing, were analyzed with this setup. Thereby very large inclusions up to several 10000 $\mu m^3$ were found at the lowest and highest temperatures. Using the crystal size distribution (CSD) approach (61; 58) the growth and nucleation rates of the voids could be extracted from the tomographic data. The results of this model agree with the growth rates of dendritic ice crystals as measured by Pruppacher (80; 81).

Furthermore, various aerosol proxies were frozen under constant conditions and mixtures of these substance were analyzed to investigate the formation and extend of networks. Clearly, a combination of sea salt and liquid organic proxies (5; 102; 103; 104; 105) can produce a highly connected structure, which will significantly alter the interactions of the particle with its surrounding gas phase or during riming.

Most of the systems studied in this work are not found in nature, where impurity concentrations are often lower. However, also natural ice is frozen from aqueous solutions leading to complex multiphase systems. The results presented here suggest that there is an interdependence of all available impurities on the micro-morphology in the multiphase system. Such effects may have a profound impact on the chemistry and transport of impurities, as such processes may occur just in the complex, three-dimensional inclusions in the ice. It is beyond the scope of this thesis to address all these issues, but future applications of micro-tomography with much higher spatial resolutions will be well suited to further explore these issues. A higher temporal resolution would significantly improve the current pseudo 4D-tomographic experiments and fully elucidate the influence of metamorphism on the morphology of the trapped inclusions and the subsequent

changes in the physico-chemical properties of the particle. The newly available high-speed tomography beam line at the SLS "TOMCAT" will be an ideal basis for such experiments. A combination of cryo-tomography and X-ray fluorescents, as already available at the ESRF, will be developed at the University at Mainz based on a commercially available bench-top tomography station.

# References


[1] S. Solomon, Progress towards a quantitative understanding of antartic ozone depletion, Nature 347 (1990) 347 – 353.

[2] J.P. Crutzen, F. Arnold, Nitric acid cloud formation in the cold antarctic stratosphere: a major cause for the springtime 'ozone hole', Nature 324 (1986) 651.

[3] T. Peter, Microphysics and heterogenous chemistry of polar stratospheric clouds, An. Phys. Chem. 48 (1997) 785 – 822.

[4] J. Seinfeld, S. Pandis, Atmospheric Chemistry and Physics, Wiley Interscience, 1997.

[5] Y. Rudich, Laboratory perspectives on the chemical transformations of organic matter in atmospheric particles, Chem. Rev. 103 (2003) 5097 – 5124.

[6] E. Meretebild, B. Svenningsson, CCN activation of slightly soluble organics: the importance of small amounts of inorganic salt and particle phase, Tellus 12 (2004) 1 – 5.

[7] G. M. Marion, A molal-based model for strong acid chemistry at low temperatures (<200 to 298 K), Geochim. Cosmochim. Acta 66 (14) (2002) 2499 – 2516.

[8] H. Eicken, C. Bock, R. Wittig, H. Miller, H. Poertner, Magnetic resonance imaging of sea-ice pore fluids: methods and thermal evolution of pore microstructure, Cold Reg. Sci. Tech. 31 (Z2000) (2000) 207–225.

[9] G. Gross, C.-H. Wu, C. McKee, Concentration dependent solute redistribution at the ice/water phase boundary. II Experimental investigation, J. Chem. Phys. 62 (8) (1975) 3085 – 3093.

[10] G. Gross, P. Wong, K. Humes, Concentration dependent solute redistribution at the ice-water phase boundary. III. Spontaneous convection. Chloride solutions, J. Chem. Phys. 67 (11) (1977) 5264 – 5275.

[11] R. Gao, J. Popp, D. Fahey, T. Marcy, R. Herman, E. Weinstock, D. Baumgartner, T. Garett, K. Rosenlof, T. Thompson, P. Bui, B. Ridley, S. Wolfsky, O. Toon, M. Tolbert, B. Kaercher, T. Peter, P. Hudson, A. Weinhiemer, A. Hemysfield, Evidence that nitric acid increases relative humidity in low-temperature cirrus clouds, Science 303 (1997) 516 – 521.

[12] P. Jungwirth, D. Rosenfeld, V. Buch, A possible new molecular mechanism of thundercloud electrification, Atmos. Res. 76 (2005) 190 – 205.

[13] M. Legrand, J. Delmas, R. Charlson, Climate forcing implications from Vostok ice core sulfate data, Nature 334 (6181) (1988) 418 – 420.

[14] B. Stauffer, Cornucopia ice core results, Nature 399 (6735) (1999) 412 – 413.

[15] C. Louis, J. Jouzel, D. Raynaud, J. Hansen, H. Le Treut, The ice core record: Climate sensitivity and future greenhouse warming, Nature 347 (6289) (1990) 139 – 147.

[16] A. W. Rempel, J. S. Wettlaufer, Anomalous diffusion of multiple impurity species: Predicted implications for the ice core climate records, J. Geophys. Res. 107 (B12) (2002) 2330.

[17] H. Pruppacher, J. Klett, Microphysics of clouds and precipiation, Kluwer Academic Publishers, 1997.

[18] D. Jacob, Introduction to atmospheric chemistry, Princeton University Press, 1999.

[19] K. Carslaw, T. Peter, Uncertainties in reactive uptake coefficients for solid stratospheric particles: I. Surface chemistry, Geophys. Res. Lett. 24 (14) (1997) 1743 – 1746.

[20] S. Clegg, J. Seinfeld, Thermodynamic models of aqueous solutions containing inorganic electrolytes and dicarboxylic acids at 298.15 K I. The acids as non-dissociating components, Phys. Chem. A. 110 (2006) 5692 – 5717.

[21] S. Clegg, J. Seinfeld, Thermodynamic models of aqueous solutions containing inorganic electrolytes and dicarboxylic acids at 298.15 K II. Systems including dissociation equilibria, Phys. Chem. A. 110 (2006) 5718 – 5734.

[22] S. Clegg, P. Brimblecombe, Application of a multicomponent thermodynamic model to activities and thermal properties of 0-40 mol kg-L aqueous sulfuric acid from 200 to 328 K, J. Chem. Eng. Data 40 (1995) 43 – 64.

[23] S. Clegg, P. Brimblecombe, A. Wexler, Thermodynamic model of the system $H^+$ - $NH_4^+$ - $SO_4^{2-}$ - $NO_3^-$ - $H_2O$ at tropospheric temperatures, J. Phys. Chem. A 102 (1998) 2137 – 2154.

[24] S. Clegg, P. Brimblecombe, Equilibrium partial pressures and mean activity and osmotic coefficients of 0 - 100% nitric acid as a function of temperature, J. Phys. Chem. 94 (1990) 5369 – 5380.

[25] W. Lyons, K. Welch, G. Snyder, J. Graham, G. Marion, R. Poreda, Halogen geochemistry of the McMurdo dry valleys lakes, Antarctica: Clues to the origin of solutes and lake evolution, Geochim. Cosmochim. Acta 69 (2) (2005) 43210 – 41002.

[26] G. Marion, D. Catling, J. Kargel, Modeling aqueous ferrous iron chemistry at low temperatures with application to mars, Geochim. Cosmochim. Acta 67 (22) (2003) 4215 – 4266.

[27] G. Marion, J. Kargel, D. Catling, Jakubowski, Effects of pressure on aqueous chemical equilibria at subzero temperatures with application to europa, Geochim. Cosmochim. Acta 69 (2) (2005) 259 –274.

[28] T. Huthwelker, M. Ammann, T. Peter, The uptake of acidic trace gases on ice, Chem. Rev. 106 (2006) 1375 – 1440.

[29] A. Borovoi, N. Kustova, Statistical approach to light scattering by convex ice crystals, Opt. Lett. 31 (11) (2006) 1747 – 1750.

[30] L. Liu, M. Mishchenko, B. Cairnsa, B. Carlson, L. Travis, Modeling single-scattering properties of small cirrus particles by use of a size-shape distribution of ice spheroids and cylinders, J. Quant. Spec. Rad. Transfer 101 (2006) 488– 497.

[31] V. Shcherbakov, J.-F. Gayet, O. Jourdan, J. Strom, A. Minikin, Light scattering by single ice crystals of cirrus clouds, Geophys. Res. Lett. 33 (2006) L15809 – L15814.

[32] P. Hobbs, Ice Physics, Clarendon Press, Oxford, 1974.

[33] V. F. Petrenko, R. Whitworth, Physics of ice, Oxford Univ. Press, 1999.

[34] S. Engemann, H. Reicher, H. Dosch, J. Bilgram, V. Honkimi, A. Snigirev, Interfacial melting of ice in contact with $SiO_2$, Phys. Res. Lett. 92 (20) (2004) 205701 – 205704.

[35] H. Dosch, A. Lied, J. Bilgram, Disruption of the hydrogen-bonding network at the surface of ih ice near surface premelting, Surf. Sci. 366 (1996) 43 – 50.

[36] H. Dosch, A. Lied, J. Bilgram, Glancing-angle x-ray scattering studies of the premelting of ice surfaces, Surf. Sci. 327 (1995) 145 – 164.

[37] A. Lied, H. Dosch, J. Bilgram, Surface melting of ice ih single crystals revealed by glancing angle x-ray scattering., Phys. Rev. Lett. 72 (22) (1994) 3554 – 3558.

[38] L. F. Voss, B. F. Henson, K. R. Wilson, J. M. Robinson, Atmospheric impact of quasiliquid layers on ice surfaces, Geophys. Res. Lett. 32 (2005) L07807 – L07810.

[39] V. Koren, Paramterization of frozen ground effects: Sensitivity to soil properties, IAHS-AISH Publications (2006) 125 – 133.

[40] N. Sghaier, M. Prat, S. B. Nasrallah, On the influence of sodium chloride concentration on equilibrium contact angle, Chem. Eng. J. 122 (2006) 47 – 53.

[41] P. Morkved, P. Doersch, T. Henriksen, L. Bakken, $N_2O$ emissions and product ratios of nitrification and denitrification as affected by freezing and thawing, Soil Biol. Biochem. 38 (12) (2006) 3411 – 3420.

[42] M. Freppaz, B. Williams, A. Edwards, R. Scalenghe, E. Zanini, Simulating soil freeze/thaw cycles typical of winter alpine conditions: Implications for N and P availability, Appl. Soil Ecol. 35 (1) (2007) 247 – 255.

[43] L. E. Wells, J. W. Deming, L. E. Wells, J. W, Viruses in winter sea ice, Environ. Microbiol. 8 (6) (2005) 1462 – 2912.

[44] J. ValenzaII, G. Scherer, Mechanism for salt scaling, J. Am. Ceram. Soc. 89 (4) (2006) 1161 – 1179.

[45] C. Knight, N. Knight, Spongy hail stone growth criteria I. Orientation fabrics, J. Atmos. Sci 25 (1968) 445 – 453.

[46] C. Knight, N. Knight, Spongy hail stone growth: II. Microstructures, J. Atmos. Sci. 25 (1968) 445 – 452.

[47] C. Knight, D. Ehhalt, N. Roper, N. Knight, Radial and tangential variation of deuterium in hail stones, J. Amos. Sci. 32 (1975) 1990 – 2000.

[48] C. Kinght, N. Knight, K. Kime, Deuterium contents of strom inflow and hail stone growth layers, J. Atmos. Sci. 38 (1981) 2485 – 2499.

[49] M. R. Stolz, M. Ram, Using laser-light scattering to measure impurities, bubbles, and imperfections in ice cores, J. Geophys. Res. 110 (2005) D11209.

[50] F. Prodi, Measurements of local density in artificial and natural hailstones, Appl. Meteo. 9 (1970) 903–910.

[51] H. Mader, Observations of the water-vein system in polycrystaline ice, J. Glac. 38 (1992) 333 – 347.

[52] L. Keyser, M. Leu, Morphology of nitric-acid and water ice films, Microsc. Res. Tech. 25 (1993) 434 – 438.

[53] P. Barnes, R. Mulvaney, E. W. Wolff, K. Robinson, A technique for the examination of polar ice using the scanning electron microscope, J. Micros. 205 (2002) 118 – 124.

[54] P. Barnes, E. Wolff, D. Mallard, H. Mader, SEM studies of the morphology and chemistry of polar ice, Mic. Res. Tech. 2 (2003) 62 –69.

[55] R. Mulvaney, E. Wolff, K. Oates, Sulphuric acid at grain boundaries in antartic ice, Nature 331 (1988) 247 –249.

[56] H. Fukazawa, K. Sugiyama, S. Mae, Acid ions at triple junction reaction of $ClONO_2$ with $H_2O$ and HCl in sulfuric acid $HNO_3/H_2SO_4/H_2O$ mixtures, J. Phys. Chem. 102 (D2) (1998) 4794 – 4807.

[57] H. Ohno, M. Igarashi, T. Hondoh, Salt inclusions in polar ice core: Location and chemical form of water-soluble impurities, Earth Planet. Sci. Lett. 232 (2005) 171–178.

[58] B. Marsh, Crystal size distribution (CSD) in rocks and the kinetics and dynamics of crystallization. I. Theory, Contrib. Minearl. Petrol. 99 (1988) 277 – 291.

[59] M. J. Zieg, B. D. Marsh, M. K. Blaustein, Crystal size distributions and scaling laws in the quantification of igneous textures, J. Petrol. 43 (1) (2002) 85 – 101.

[60] M. J. Zieg, G. E. Lofgren, An experimental investigation of texture evolution during continuous cooling, J. Volcan. Geotherm. Res. 154 (2006) 10 – 17.

[61] A. Randolph, M. Larson, Theory of particulate processes, Academic, Press, New York, 1971.

[62] E. Tuduri, R. Romero, L. Lopez, E. Garcia, J. Sanchez, C. Ramis, The 14 Juli 2001 hailstorm in northeastern Spain: Diagnosis of meteorological situation, Atmos. Res. 67 (8) (2003) 541 – 558.

[63] D. Pocakal, J. Stalec, Statistical analysis of hail characteristics in the hail-protected western part of Croatia using data from hail suppression stations, Atmos. Res. 67-68 (2003) 533 – 540.

[64] R. Farley, H. Chen, H. Orville, M. Hjelmfelt, Numerical simulation of hail formation in the 28 June 1989 Bismarck thunderstorm. Part I. Studies related to hail production, Atmos. Res. 71 (2004) 51 – 79.

[65] J. Sanchez, M. Fernandez, J. Fernandez, E. Tuduri, C. Ramis, Analysis of mesoscale convective systems with hail precipitation, Atmos. Res. 67-68 (2003) 573 – 588.

[66] X. Guo, M. Huang, Hail formation and growth in a 3D cloud model with hail-bin microphysics, Atmos. Res. 63 (2002) 59 – 99.

[67] N. Castellano, O. Nasello, Comments about the drag laws used in hail growth simulations, Atmos. Res. 43 (1997) 315 – 323.

[68] K. Cashman, B. Marsh, Crystal size distribution (CSD) in rocks and the kinetics and dynamics of crystallization II: Makaopuhi lava lake, Contrib. Mineral. Petrol. 99 (1988) 292 – 305.

[69] M. Hounslow, G. Reynolds, Product engineering for crystal size distribution, AIChe 52 (7) (2006) 2507 – 2517.

[70] M. Schneebeli, A. Sokratov, Tomography of temperature gradient metamorphism of snow and associated changes in heat conductivity, Hydr. Proc. 18 (2004) 3655 – 3665.

[71] J. Brzoska, C. Colu, B. Lesaffre, S. Borel, O. Brissaud, W. Ludwig, E. Boller, J. Baruchel, 3D visualization of snow samples by microtomography at low temperature, ESRF Newsletter (1999) 22 – 23.

[72] F. Flin, J. Brzoska, B. Lesaffre, C. Coleou, P. Lamboley, Computation of normal vectors of discrete 3D Objects: Application to natural snow images from X-ray tomography, Image Anal. Stereol. 20 (2001) 187 – 191.

[73] F. Flin, J. Brzoska, B. Lesaffre, C. C., R. Pieritz, Full three dimensional modelling of curvature dependent snow metamorphism: First results and comparison with experimental tomographic data, J. Phys. D: Appl. Phys. 36 (2003) A49 – A54.

[74] M. Miedaner, T. Huthwelker, F. Enzmann, M. Stampanoni, M. Kersten, M. Ammann, A new setup for synchrotron micro-cryo-tomography of ice particles and their metamorphism, Mic. Res. Tech. (2007) submitted.

[75] S. Colbeck, Theory of metamorphism of dry snow, J. Geophys. Res. 88 (C9) (1983) 5475 – 5482.

[76] F. Domine, T. Lauzier, A. Cabanes, L. Legagneux, W. F. Kuhs, K. Techmer, T. Heinrichs, Snow metamorphism as revealed by scanning electron microscopy, Mic. Res. Tech. 62 (2003) 33 – 48.

[77] A. Cabanes, L. Legagneux, F. Domine, Rate of evolution of the specific surface area of surface snow layers, Environ. Sci. Tech. 37 (4) (2003) 1 – 10.

[78] M. Miedaner, T. Huthwelker, M. Stampanoni, F. Enzmann, M. Kersten, M. Ammann, A. Groso, M. Stampanoni, Characterization of temperature dependend impurity trapping by ice, Crystal Growth.

[79] T. Koop, B. Luo, A. Tsias, Water activity as the determinant for homogeneous ice nucleation in aqueous solutions., Nature 406 (2000) 611–614.

[80] H. Pruppacher, Some relations between the structure of the ice-solution interface and the free growth rate of ice crystals in supercooled aqueous solutions., J. Coll. Interf. Sci. 25 (1967) 285–294.

[81] H. Pruppacher, Interpretation of experimentally determined growth rates of ice crystals in supercooled water., J. Chem. Phys. 47 (5) (1967) 1807–1813.

[82] M. Miedaner, T. Huthwelker, F. Enzmann, M. Stampanoni, M. Kersten, M. Ammann, Characterization of impurities in ice, Royal Chem. Soc. Proc. PCICE2006 (2007) in press.

[83] M. Stampanoni, G. Borchert, P. Wyss, R. Abela, B. Patterson, S. Hunt, D. Vermeulen, P. Rueeggsegger, High resolution X-ray detector for synchrotron-based micro tomography, Nuc. Instr. Meth. Phys. Res. A 491 (2002) 291 – 301.

[84] J. Radon, über die Bestimmung von Funktionen durch ihre Integralwerte längs gewisser Mannigfaltigkeiten, Ber. Verb. Saechs. Akad. Wiss., Leipzig, Math. Phys. Kl. 69 (1917) 262 – 277.

[85] G. Herman, Image reconcstruction from projections, Academic Press, 1980.

[86] D. Stauffer, A. Aharony, Introduction to Percolation Theory, London: Taylor and Francis, 1992.

[87] H. Wadell, Spericity and roundness of rock particles, J. Geol. 41 (1933) 310.

[88] S. Brunauer, R. Mikhail, E. Bodor, Pore Structure Analysis without a Pore Shape Model, J. Coll. Interf. Sci. 24 (1967) 451–463.

[89] S. Lowell, J. Shields, M. Thomas, M. Thommes, Characterization of porous solids and powders: Surface area, pore size and density, Kluwer Academic Press, 2004.

[90] M. Higgins, Measurement of crystal size distributions, Am. Min. 85 (2000) 1105 – 1116.

[91] G. Brandeis, C. Jaupart, The kinetics of nucleation and crystal growth and scaling laws for magmatic crystallization, Contrib. Mineral. Petrol. 96 (1987) 24 – 34.

[92] A. Carte, Air bubbles in ice, Proc. Phys. Soc. 77 (1961) 757 – 770.

[93] J. H. Seinfeld, Clouds, contrails and climate, Nature 391 (3) (1998) 837.

[94] L. Legagneux, T. Lauzier, F. Dominé, W. Kuhs, T. Heinrichs, K. Techner, Rate if decay of specific surface area of snow during isothermal experimetns and morphological changes studied by scanning electron microscopy, Can. J. Phys. 81 (2003) 459 – 468.

[95] C. Saunders, E. Avila, S. Peck, N. Castellano, G. Aguirre Varela, A laboratory study of the effects of rime ice accretion and heating on charge transfer during ice crystal graupel collisions, Atmos. Res. 51 (1999) 9 – 117.

[96] C. Saunders, A. Hosseini, A laboratory study of the effect of velocity on Hallett-Mossop ice crystal multiplication, Atmos. Res. 59-60 (2001) 3 – 14.

[97] C. Saunders, S. Peck, G. Aguirre Varela, E. Avila, N. Castellano, A laboratory study of the influence of water vapour and mixing on the charge transfer process during collisions between ice crystals and graupel, Atmos. Res. 58 (2001) 187 – 203.

[98] S. Colbeck, Statistics of coarsening inn water-saturated snow, Acta Metall. 34 (3) (1986) 347 – 352.

[99] S. Colbeck, Theory of particle coarsening with a log-normal distribution, Acta Metall. 35 (7) (1987) 1583 – 1588.

[100] P. D. Taylor, D. L. Feltham, A model of melt pond evolution on sea ice, J. Geophys. Res. 109 (2004) C12007.

[101] D. Lide, CRC Chemistry and Physics Handbook, CRC Press, 2004.

[102] J. Sun, P. A. Ariya, Atmospheric organic and bio-aerosols as cloud condensation nuclei (CCN): A review, Atmos. Environ. 40 (2006) 795 – 820.

[103] H. Z. Zhang, Y. Q. Li, P. Davidovits, Uptake of gas-phase species by 1-octanol. 2. uptake of hydrogen halides and acetic acid as a function of relative humidity and temperature, J. Phys. Chem. A 107 (2003) 6398 – 6407.

[104] R. Atkinson, J. Arey, Gas-phase tropospheric chemistry of biogenic

volatile organic compounds: a review, Atmos. Environ. 37 (2) (2003) 197 – 219.

[105] A. Motelay-Massei, T. Harner, M. Shoeib, M. Diamond, G. Stern, B. Rosenberg, Using passive air samplers to assess urban rural trends for persistent organic pollutants and polycyclic aromatic hydrocarbons. 2. Seasonal trends for PAHS, PCBS and organochlorine pesticides, Environ. Sci. Tech. 39 (2005) 5763 – 5773.

[106] R. List, Kennzeichen atmosphärischer Eispartikel 1. Teil Graupeln als Wachstumszentren von Hagelkörnern, Z. Angew. Math. Phys. 9 (2) (1958) 180.

[107] R. List, Kennzeichen atmosphärischer Eispartikeln 2. Teil Hagelkörner, Z. Angew. Math. Phys. 9 (1958) 217.

[108] L. Levi, Interpretation of the orientation of ice dendrites growing from supercooled water, J. Glaciol. 9 (1970) 109.

[109] W. Macklin, P. Rye, Crystallographic orientation distributions in accreted ice, J. Atmos. Sci. 31 (1974) 849.

[110] J.-S. Wey, J. Estrin, Modeling the batch crystallization process. The ice-brine system, Ind. Eng. Chem. Process Des. Develop. 12 (3) (1972) 236 – 240.

[111] M. G. Worster, Natural convection in a mushy layer, Science 224 (1991) 335 – 359.

[112] M. G. Worster, Instabilities of the liquid and mushy regions during solidification of alloys, J. Fluid Mech. 237 (1992) 649 – 669.

[113] M. G. Worster, J. S. Wettlaufer, Natural convection, solute trapping, and channel formation during solidification of saltwater, J. Phys. Chem. B 101 (1997) 6132 – 6136.

[114] A. W. Rempel, J. S. Wettlaufer, Interfacial premelting and the thermomolecular force: Thermodynamic buoyancy, Phys. Rev. Lett. 87 (8) (2001) 1 – 7.

[115] L. Benatov, J. S. Wettlaufer, Abrupt grain boundary melting in ice, Phys. Rev. E 70 (2004) 061606 – 061613.

[116] S. Davis, Theory of solidification, Cambridge University Press, 1980.

[117] A. W. Rempel, M. G. Worster, The interaction between a particle and an advancing solidification front, J. Cryst. Growth 205 (1999) 427 – 440.

[118] M. Mangan, K. Cashman, The strucutre of basaltic scoria and reticulite and inferences for vesiculation, foam formation, and fragmentation in lava fountains, J. Volc. Geotherm. Res. 73 (1996) 1 – 18.

[119] T. Koop, B. Luo, A. Tsias, T. Peter, Water activity as the determinant for homogeneous ice nucleation in aqueous solutions, Nature 406 (2000) 611 – 615.

[120] D. Anderson, A model for diffusion-controlled solidification of ternary alloys in mushy layers, J. Fluid Mech. 483 (2003) 165 – 197.

[121] D. Anderson, M. Worster, A new oscillatory instability in a mushy layer during the solidification of binary alloys, J. Fluid Mech. 307 (1996) 245 – 267.

[122] D. Anderson, M. Worster, Weakly nonlinear analysis of convection in mushy layers during the solidification of binary alloys, J. Fluid Mech. 302 (1995) 307 – 331.

[123] P. Aussillous, A. Sederman, L. Gladden, H. Huppert, M. Worster, Magnetic resonance imaging of structure and convection in solidifying mushy layers, J. Fluid Mech. 552 (2006) 99 – 125.

[124] D. Notz, M. G. McPhee, M. G. Worster, G. A. Maykut, K. H. Schlunzen, H. Eicken, Impact of underwater-ice evolution on arctic summer sea ice, J. Geophys. Res. 108 (C7) (2003) 3223.

[125] T. P. Schulze, M. G. Worster, A time-dependent formulation of the mushy-zone free-boundary problem, J. Fluid Mech. 541 (2005) 193 – 202.

[126] T. P. Schulze, M. G. Worster, Weak convection, liquid inclusions and the formation of chimneys in mushy layers, J. Fluid Mech. 388 (1999) 197 – 215.

[127] T. P. Schulze, M. G. Worster, A numerical investigation of steady convection in mushy layers during the directional solidification of binary alloys, J. Fluid Mech. 356 (1998) 199 – 220.

[128] T. G. L. Shirtcliffe, H. E. Huppert, M. G. Worster, Measurement of the solid fraction in the crystallization of a binary melt, J. Cryst. Growth 113 (1991) 566 – 574.

[129] A. F. Thompson, H. E. Huppert, M. G. W. and. A. Liaitta, Solidification and compositional convection of a ternary alloy, J. Fluid Mech. 497 (2003) 167 – 199.

[130] J. S. Wettlaufer, M. G. Worster, H. E. Huppert, Natural convection during solidification of an alloy from above with application to the evolution of sea ice, J. Fluid Mech. 344 (1997) 291 – 316.

[131] M. G. Worster, R. C. Kerr, The transient behaviour of alloys solidified from below prior to the formation of chimneys, Science 269 (1994) 23 – 44.

[132] A. L. Stuart, M. Z. Jacobson, A numerical model of the partitioning of trace chemical solutes during drop freezing, Journal of Atmospheric Chemistry 53 (2006) 13 – 42.

[133] O. Weinstein, S. Brandon, Dynamics of partially faceted melt/crystal interfaces II: Multiple step source calculations, J. Cryst. Growth 270 (2004) 972 – 974.

[134] C. Weiss, N. Bergeon, N. Mangelinck-Noel, B. Billia, Effects of the interface curvature on cellular and dendritic microstructures, Mater. Sci. Eng., A 413414 (2005) 296 – 301.

[135] E. Petrishcheva, J. Renner, Two-dimensional analysis of pore drag and drop, Acta Mater. 53 (2005) 2793 – 2803.

[136] J. S. Wettlaufer, M. G. Worster, H. E. Huppert, Solidification of leads: Theory, experiment, and field observations, Geophys. Res. 105 (C1) (2000) 1123 – 1134.

[137] J. S. Wettlaufer, M. G. Worster, L. A. Wilen, Premelting dynamics: Geometry and interactions, J. Phys. Chem. B 101 (96) (1997) 6137 – 6141.

[138] H. Afeefy, J. Liebman, S. Stein, Neutral Thermochemical Data in NIST Chemistry WebBook, NIST Standard Reference Database, no. 69, National Institute of Standards and Technology, Gaithersburg MD, 20899, 2005.

[139] A. W. Rempel, M. G. Worster, Particle trapping at an advancing solidification front with interfacial-curvature effects, J. Cryst. Growth 223 (2001) 420 – 432.

[140] S. Colbeck, Temperature dependence of the equilibrium form of ice, J. Cryst. Growth 72 (1985) 726 – 732.

[141] W. Beckmann, Interface kinetics of the growth and evaporation of ice single crystals from the vapour phase III. Measurements under partial pressures of nitrogen, J. Cryst. Growth 58 (1982) 443 – 451.

[142] B. Mutaftschiev, The atmostic nature of crystal growth, Springer Verlag, Berlin - Heidelberg, 2001.

[143] M. Bostrom, D. Williams, B. Ninham, Surface tension of electrolytes: Specific ion effects explained by dispersion forces, Langmuir 17 (2001) 4475 – 4478.

[144] M. Bostrom, W. Kunz, B. Ninham, Hofmeister effects in surface tension of aqueous electrolyte solution, Langmuir 21 (2005) 2619 – 2623.

[145] H. Herrmann, D. Hong, H. Stanley, Backbone and elastic backbone of percolation clusters obtained by the new method of "burning", J. Phys. A: Math. Gen. 17 (1984) L261 – L266.

[146] M. Proto, A. Bunde, S. Havlin, H. Roman, Structural and dynamical properties of percolation backbone in two and three dimensions, Phys. Rev. E 56 (2) (1997) 1667 – 1676.

[147] D. Hader, Image Analysis: Methods and Applications, Second Edition, CRC, 2000.

[148] M. Seul, L. O'Gorman, M. Sammon, Practical Algorithms for Image Analysis: Descriptions, Examples, and Code, Cambridge University Press, 2000.

[149] T. Yoo, Insight into Images: Principles and Practice for Segmentation, Registration, and Image Analysis, AK Peters, 2004.

[150] S. Skiena, The Algorithm Design Manual, Springer, 1998.

[151] A. Cline, R. Renka, A storage-efficient method for construction of a Thiessen triangulation, Rocky Mountain J. of Math. 14 (1984) 119 – 139.

[152] A. Cline, R. Renka, A triangle $C^1$ interpolation method, Rocky Mountain J. of Math. 14 (1984) 223 – 237.

[153] L. Schumaker, Triangulation methods, Academic Press, New York, 1987.

[154] M. Hussmann, Ein Triangulierungsverfahren zur Approximation mit Dahmen-Micchelli-Seidel-Splines, Ph.D. thesis, University Duisburg (1999).

[155] E. Quaisser, Diskrete Geometrie, Spektrum Akademischer Verlag, Heidelberg, 1984.

[156] F. Preparata, M. Shamos, Computational Geometry, Springer, New York, 1985.

[157] G. Aummann, K. Spitzmueller, Computer Orientierte Geometrie BI, Wissenschaftsverlag, Mannheim, 1993.

# A Appendix

All tomographic data were analyzed using the AMIRA software package (Mercury Systems). This commercial suite of programs provides the user with a well designed manual that explains the detailed usage of most of the components. However, neither mailing lists and a scientific documentation nor a listing of the employed algorithm are available. Additionally, Mercury Systems does not answer such requests. Therefore, a short description of the principle of a burning and a triangulation algorithm will be given in the following. These descriptions do not provide a detailed review of the implementation into AMIRA, but they show the principle of operation on which the used routines were based.

## A.1 Comments on the "burning algorithm"

The burning algorithm has been widely used to identify connected voxels or pixels in 3D and 2D data sets (86; 145; 146; 147; 148; 149; 150, and references therein). Based on it output various information like its fractal component, volume etc. of the identified object could be gained.
This algorithm starts on a simplified matrix, which was constructed by the threshold segmentations. There, all voxels representing a certain substance (air, salt or ice) were extracted from the complete tomographic data set. The result was stored in a matrix of the same dimensions as the input data, but its content was reduced to a value of 0 for non-segmented and to a value of 1 for segmented volume elements. For simplicity the 0-voxels will be called "background" and the 1-voxels will be called "object". Starting from a randomly chosen point the burning algorithm (86; 146) moved a kernel of predefined size (3 to 5 in AMIRA) through the matrix looking for an object-voxel. Once such an element had been found, a new object (numbered) was added to the table summarizing the connected components. Then the neighbors of the just found voxel were investigated according to a user-defined degree of connectivity. AMIRA offered to investigated up to 26

possible neighbors. This maximum was used in all analyses performed in this study. Every identified object-voxel was "burned", meaning its coordinates were added to the object in the table of connected components. After all voxels sharing at least one side were burned this algorithm closed the object and moved forward through the matrix for the next object-voxel. After having seen the whole matrix, a second matrix of the same dimensions was generated consisting of 0-values for the background and the voxels of each object were assigned the number of the object. A visualization of such a matrix would result in a maximum of 255 objects (a ridiculous constraint by AMIRA, because an unlimited amount of objects would be possible by a hard-swap of this table to the hard disk) each appearing in its own color. Various improvements, like starting the "burning algorithm" in the top right corner and comparing its results to the ones obtained from starting in the opposite corner, loop-based runs, parallel and different sequential runs, etc. were described in the literature (86; 145; 146). These were mainly used to calculate the percolation properties of the substance investigated. The pores in the ice samples, however, were all isolated. Therefore the use of the "burning algorithm" was only required to obtain the geometrical data of the single inclusions. A further detailed discussion on the variations of this algorithm and other approaches of image analysis can be found in the literature (86; 147; 148; 149; 150).

## A.2 Comments on the triangulation algorithm

A large number of triangulation algorithms has been developed during the last 20 years (151; 152; 153). Since neither AMRIA itself, nor Mercury Systems provide any information which algorithm is used for triangulation, a short and simple method will be presented to recall the basic concept of this process. A greater discussion of triangulation algorithms can be found in the PhD thesis of Markus Hussmann (154). The following description is based on his work.

Triangulation is the art of creating the complex surface of a diffuse cloud of points in three or two dimensional space by setting up triangles or polygones. Various criteria have been developed to evaluate to what extend the triangulated surface represents the real shape of the objects and which number of triangles can be reduced. The tomographic data obtained in this study can be imagined as a cloud of voxels having different values. This picture can be simplified by threshold segmentation and the use of the burning algorithm. Furthermore, it is assumed that only one segmented and burned object shall be triangulated. As a first step one axis of the coordinate system has to be chosen (e.g. x-axis). The voxels having the minimal and maximal coordinates on this axis (V1 and V2), respectively, have to be found. These points set up a line that splits the voxel-cloud within a chosen plane (e.g.: xy-plane) into two parts. Now all voxels on one side of the line will be sorted in ascending distance from V1 and on the other side in descending distance with respect to V2. Starting form V1 to V2 the algorithm connects all voxels with a line. Voxels which indicate a step backward, will be deleted. Since the surface of the object shall be represented by triangles, two point on the just created hull are picked as long as the are connected by straight line. A third point within the current plane or outside of it has to be chosen. Thereby the following criteria applies. All three points, forming a triangle, have to lie on the same circumscribed circle. Additionally the internal angles of this structure shall

be maximized. Once the first triangle is build in this way, two of its points will be the base for the next. Points which fall within one of the thus formed triangles will be deleted. After the first triangulation run, when no free object-voxels exist anymore, different optimization algorithms can be added to improve the surface representation and to reduce the final amount of triangles needed and so to optimize the consumption of memory.
Clearly, this is a very simplistic algorithm to describe triangulation, but due to the lack of information caused by Mercury Systems only speculations about the implemented algorithm are possible. More complex and efficient approaches than the one presented above can be found in the literature (147; 148; 149; 150; 151; 152; 153; 155; 156; 157).

## A.3 Routines developed for tomography data analysis

### A.3.1 Technical notes

The source code of the software discussed in this section is available at: http://www.rootshell.be/∼miedaner/tools.tar.gz. Detailed information about its copyright can be found at: http://www.gnu.org/copyleft/gpl.html.
The C/C++-codes are written in such a way that they may also be compiled on a Windows-system - this however was never intended. Please note that this is free-software (GPL-V2) and the author cannot be held responsible for absolutely any damage that occurs to the reader, user or any computer due to the use or reading of these computer codes.

### A.3.2 Description and usage

Once less than 256 objects were identified using the burning-algorithm (86), their surface area as well as their volume were determined with the triangulation routines provided by AMIRA Software Package (Mercury Systems). The thus obtained data were stored as tables in ASCII-format (mainly CSV, or TXT) and moved to a GNU-DEBIAN system (testing) for further analysis with the routines presented below. Different combinations of the separately compiled routines and bash-scripts allowed a fast and

simple analysis of the experimental data. Please note that all routines use the output files of tab2raw.sh and do not depend on each other.

- tab2raw.sh
  This is the main file. It opens the tables created by AMIRA and extracts the individual data of each object into one file for volume and one file for surface area. Afterwards various routines can be started.

- simple-area.cpp
  This routine opens the raw surface area data file created by tab2raw.sh and recalculates all measurements as $\mu m^2$. It also generates a cumulative distribution of the surface area data.

- simple-volume.cpp
  This routine performs the same task as simple-area.cpp but for the volume data.

- simple-analysis.cpp
  This routine determines the total, average, minimum and maximum volumes and surface areas of the data set, as well as the standard deviations of these values.

- simple-sphere-waldell.cpp
  This routine calculates to what extend each object deviates from an ideal spherical geometry according to the approach of Waldell (87).

**Filename: tab2raw.sh**

```
#!\bin\bash
# ----------------
# Copyright of this script -> GPL-V2
# ----------------
for ff in *; do
```

```
sed -n '/Material-/p' $ff > $ff'.out'
done
mkdir output
mv *.out output/
cd output
for filename in *; do
unexpand $filename | cut -f3 -s > $filename'.area'
unexpand $filename | cut -f4 -s > $filename'.volume'
done
for file in f*.area; do
less $file — tee -a area.dat
done
for file2 in f*.volume; do
less $file2 — tee -a volume.dat
done
# add routines for further analysis here:
# simple-area
# simple-volume
# etc.

cd ..
clear
echo "Done! Data are extracted from original data. Output can be found at ./output including summary files: area.dat and volume.dat"
```

**simple-area.cpp** // COPYRIGHT –> GPL-V2

```
#include<iostream>
#include<iomanip>
```

```
#include<fstream>
#include<algorithm>
using namespace std;
// global variables
int main(){
// local variables
float areararaw[10000];
float area[10000];
float sum[10000];
float total=0;
float areapercentage[10000];
int a=0;
int b=0;
// open file and read all data into array area[]
fstream InFile;
InFile.open("area.dat", ios::in);
if (InFile.fail()){
cout << "Unable to open Inputfile";
exit(1);
}
while (! InFile.fail()){
InFile >> areararaw[b];
b++;
}
// close the file again
InFile.close();
// recalculate everything in micro meters.
while ( a < b){
area[a] = (areararaw[a] * 1.4 * 1.4);
sum[a] = sum[a-1] + area[a];
total = total + area[a];
```

```
a++;
}
// sort data and calculate area percentage in equiv array.
sort(area, area+b+1);
areapercentage[0] = (area[0] / total ) * 100;
a = 1;
while ( a < b + 1){
areapercentage[a] = areapercentage[a-1] + ( area[a] / total) * 100;
a++;
}
// make sure that area and areaprecentage have the same order.
sort(areapercentage, areapercentage+7);
// write everything into a new file
fstream OutFile;
OutFile.open("area.dat.out", ios::out);
if (OutFile.fail()){
cout << "Open outputfile failed!" << endl;
exit(1);
}
a = 2; // First two elements are empty 0;0
while (a < b + 1){
OutFile << area[a] << ";" << areapercentage[a] << endl;
a++;
}
OutFile.close();
return 0;
}
```

**simple-volume.cpp**

```
// COPYRIGHT –> GPL-V2
#include<iostream>
#include<iomanip>
#include<fstream>
#include<algorithm>
using namespace std;
// global variables
int main(){
// local variables
float volumeraw[10000];
float volume[10000];
float sum[10000];
float total=0;
float volumepercentage[10000]; int a=0; int b=0; // open file and read all
data into array area[] fstream InFile;
InFile.open("volume.dat", ios::in);
if (InFile.fail()){
cout << "Unable to open Inputfile" << endl;
exit(1);
}
while (! InFile.fail()){
InFile >> volumeraw[b];
b++;
}
// close the file again
InFile.close();
// recalculate everything in micro meters.
while ( a < b){
volume[a] = (volumeraw[a] * 1.4 * 1.4 * 1.4);
sum[a] = sum[a-1] + volume[a];
```

```
total = total + volume[a];
a++;
}
// sort data and calculate volume percentage in equiv array.
sort(volume, volume+b+1);
volumepercentage[0] = (volume[0] / total ) * 100;
a = 1;
while ( a < b + 1){
volumepercentage[a] = volumepercentage[a-1] + ( volume[a] / total) * 100;
a++;
}
// make sure that volume and volumeprecentage have the same order.
sort(volumepercentage, volumepercentage+7);
// write everything into a new file
fstream OutFile;
OutFile.open("volume.dat.out", ios::out);
if (OutFile.fail()){
cout << "Open outputfile failed!" << endl;
exit(1);
}
a = 2; // First two elements are empty 0;0
while (a < b + 1){
OutFile << volume[a] << ";" << volumepercentage[a] << endl;
1cm a++;
}
OutFile.close();
return 0;
}
```

**simple-analysis.cpp**

```
// COPYRIGHT –> GPL-V2
#include<iostream>
#include<iomanip>
#include<fstream>
#include<math.h>
using namespace std;
// global variables
int main(){
// local variables
double areararaw = 0;
double area = 0;
double volumeraw = 0;
double volume = 0;
double sum_volume = 0;
double sum_area = 0;
double average_volume = 0;
double average_area = 0;
double stdev_volume_raw =0;
double stdev_volume = 0;
double stdev_area = 0;
double stdev_area_raw = 0;
double avedev_volume_raw = 0;
double avedev_volume = 0;
double abs_volume = 0;
double avedev_area_raw = 0;
double avedev_area = 0;
double abs_area = 0;
double min_volume = 0;
double min_area = 0;
double max_volume = 0;
```

```
double max_area = 0;
int a=0;
// open file and read all data into area and volume;
fstream InFile;
InFile.open("area.dat", ios::in);
if (InFile.fail()){
cout << "Unable to open Area Inputfile";
exit(1);
}
fstream InFile2;
InFile2.open("volume.dat", ios::in);
if (InFile2.fail()){
cout << "Unable to open Volume Inputfile";
exit(1);
}
while (! InFile.fail()){
area = 0;
volume = 0;
InFile >> areararaw;
area = areararaw * 1.96;
InFile2 >> volumeraw;
volume = volumeraw * 2.744;
a++;
sum_volume = sum_volume + volume;
sum_area = sum_area + area;
// set inital conditions:
if (a ==1){
max_volume = volume;
min_volume = volume;
max_area = area;
min_area = area;
```

```
}
if (volume > max_volume ){
max_volume = volume;
}
if (area > max_area){
max_area = area;
}
if (volume < min_volume){
min_volume = volume;
}
if (area < min_area){
min_area = area;
}
}
// close the file again
InFile.close();
InFile2.close();
area = areараw = 0;
volume = volumeraw = 0;
// calculate averages
average_volume = sum_volume / a;
average_area = sum_area / a;
// calculate deviation from average and standard deviation
fstream InFile3;
InFile3.open("area.dat", ios::in);
if (InFile3.fail()){
cout << "Unable to open Area Inputfile";
exit(1);
}
fstream InFile4;
InFile4.open("volume.dat", ios::in);
```

```
if (InFile4.fail()){
cout << "Unable to open Volume Inputfile";
exit(1);
}
while (! InFile3.fail()){
// get inputdata:
InFile3 >> areararaw;
area = areararaw * 1.4 * 1.4;
InFile4 >> volumeraw;
volume = volumeraw * 1.4 * 1.4 * 1.4;
// standart deviation raw:
stdev_area_raw = stdev_area_raw + pow((area - average_area), 2);
stdev_volume_raw = stdev_volume_raw + pow((volume - average_volume),
2);
// average deviation raw:
abs_area = area - average_area;
abs_volume = volume - average_volume;
if (abs_area > 0){
avedev_area_raw = avedev_area_raw + abs_area;
}
else{
avedev_area_raw = avedev_area_raw - abs_area;
}
if (abs_volume > 0){
avedev_volume_raw = avedev_volume_raw + abs_volume;
}
else{
avedev_volume_raw = avedev_volume_raw - abs_volume;
}
}
// close every thing again
```

```
InFile3.close();
InFile4.close();
// standart deviation:
stdev_area = sqrt(stdev_area_raw / (a - 1));
stdev_volume = sqrt(stdev_volume_raw / (a - 1));
// average deviation:
avedev_area = (avedev_area_raw / (a - 1));
avedev_volume = (avedev_volume_raw / (a - 1));
// write everything into a new file
fstream OutFile;
OutFile.open("analysis.dat", ios::out);
if (OutFile.fail()){
cout << "Open outputfile failed!" << endl;
exit(1);
}
OutFile <<"++++++++++++++++++++++++++++++++++" <<
endl;
OutFile << "Total Volume: " << sum_volume << endl;
OutFile << "Total Surface Area: " << sum_area << endl;
OutFile << "--------------------------" << endl;
OutFile << "Average Volume: " << average_volume << endl;
OutFile << "Average Surface Area: " << average_area << endl;
OutFile << "--------------------------" << endl;
OutFile << "Standart Deviations: " << endl;
OutFile << "Volume: " << stdev_volume << endl;
OutFile << "Surface area: " << stdev_area << endl;
OutFile << "--------------------------" << endl;
OutFile << "Deviation from Average: " << endl;
OutFile << "Volume: " << avedev_volume << endl;
OutFile << "Area: " << avedev_area << endl;
OutFile << "--------------------------" << endl;
```

```
OutFile << "Minimum Volume: " << min_volume << endl;
OutFile << "Maximum Volume: " << max_volume << endl;
OutFile << "Minium Surface Area: " << min_area << endl;
OutFile << "Maximum Surface Area: " << max_area << endl;
OutFile <<"++++++++++++++++++++++++++++++++++++++++++"
<< endl;
// close it!
OutFile.close();
// give a short summary:
cout << "++++++++++++++++++++++++++++++++++++++"
<< endl;
cout << "Total Volume: " << sum_volume << endl;
cout << "Total Surface Area: " << sum_area << endl;
cout << "-------------------------" << endl;
cout << "Average Volume: " << average_volume << endl;
cout << "Average Surface Area: " << average_area << endl;
cout << "-------------------------" << endl;
cout << "Standart Deviations: " << endl;
cout << "Volume: " << stdev_volume << endl;
cout << "Surface area: " << stdev_area << endl;
cout << "-------------------------" << endl;
cout << "Deviation from Average: " << endl;
cout << "Volume: " << avedev_volume << endl;
cout << "Area: " << avedev_area << endl;
cout << "-------------------------" << endl;
cout << "Maximum Volume: " << max_volume << endl;
cout << "Minimum Volume: " << min_volume << endl;
cout << "Maximum Surface Area: " << max_area << endl;
cout << "Minimum Surface Area: " << min_area << endl;
cout << "-------------------------" << endl;
cout << "All data are in micro-meter and " << endl;
```

```
cout << "written to analysis.dat" << endl;
cout << a << " pores analyzed. " << endl;
cout << "++++++++++++++++++++++++++" << endl;
return 0;
}
```

**simple-sphere-waldell**

```
// COPYRIGHT -> GPL-V2
#include<iostream>
#include<iomanip>
#include<fstream>
#include<math.h>
using namespace std;
// global variables
int main(){
// local variables
double areararaw;
double area;
double volumeraw;
double volume;
double deviation_from_sphere;
double a = 0.3333;
double b = 0.6666;
// open file and read all data into array area[]
fstream InFile;
InFile.open("area.dat", ios::in);
if (InFile.fail()){
cout << "Unable to open Area Inputfile";
```

```
exit(1);
}
fstream InFile2;
InFile2.open("volume.dat", ios::in);
if (InFile2.fail()){
cout << "Unable to open Volume Inputfile";
exit(1);
}
fstream OutFile;
OutFile.open("deviation_from_sphere_waldell.dat", ios::out);
if (OutFile.fail()){
cout << "Open outputfile failed!" << endl;
exit(1);
}
while (! InFile.fail()){
InFile >> areararaw;
InFile2 >> volumeraw;
area = (areararaw * 1.4 * 1.4);
volume = (volumeraw * 1.4 * 1.4 * 1.4);
// after waldell 1932:
deviation_from_sphere = (pow(3.1415, a) * pow((6 * volume), b))/area;
OutFile << deviation_from_sphere << endl;
}
// close the fileis again
InFile.close();
InFile2.close();
OutFile.close();
// and that's it ;-)
return 0;
}
```

**simple-morphanalysis.cpp**

```
// COPYRIGHT –> GPL-V2
#include<iostream>
#include<iomanip>
#include<fstream>
#include<math.h>
using namespace std;
// global variables
float data = 0;
int sphere = 0;
int szylinder = 0;
int mzylinder = 0;
int thread = 0;
int lthread = 0;
int velongated = 0;
int a = 0;
int main(){
// open file and read all data into area and volume;
fstream InFile;
InFile.open("deviation_from_sphere_waldell.dat", ios::in);
if (InFile.fail()){
cout << "Unable to open inputfile. Does it exist?" << endl;
exit(1);
}
while (! InFile.fail()){
InFile >> data;
if (data > 0.65){
sphere = sphere + 1;
}
if (data < 0.65){
if (data >0.42){
```

```
szylinder = szylinder +1;
}
}
if (data < 0.42){
if (data > 0.27){
mzylinder = mzylinder + 1;
}
}
if (data < 0.27){
if (data > 0.15){
thread = thread + 1;
}
}
if (data < 0.15){
if (data > 0.10){
lthread = lthread + 1;
}
}
if (data < 0.1){
velongated = velongated + 1;
}
a++;
}
// close the file again and calcluate average
InFile.close();
// give a short summary
cout << " Total number of pores found: " << a << endl;
cout << " Therein were: " << endl;
cout << " ----------" << endl;
cout << "Spheres: " << sphere << endl;
cout << "Small zylinders: " << szylinder << endl;
```

```
cout << "Medium zylinders: " << mzylinder << endl;
cout << "Large Zylinders: " << thread << endl;
cout << "Threads: " << lthread << endl;
cout << "Long threads: " << velongated << endl;
// write everything into a new file
fstream OutFile;
OutFile.open("morphology.out", ios::out);
if (OutFile.fail()){
cout << "Unable to open outputfile. No space left? " << endl;
exit(1);
}
OutFile << "Spheres: " << sphere << endl;
OutFile << "Small zylinders: " << szylinder << endl;
OutFile << "Medium zylinders: " << mzylinder << endl;
OutFile << "Large Zylinders: " << thread << endl;
OutFile << "Threads: " << lthread << endl;
OutFile << "Long threads: " << velongated << endl;
// close streams!
OutFile.close();
cout << " All data were written to: morphology.out ." << endl;
return 0;
}
```